



**HAL**  
open science

## **Ionic columnar clustomesogens associations between anionic hexanuclear rhenium clusters and liquid crystalline triphenylene tethered imidazoliums**

F Camerel, F Kinloch, O Jeannin, M Robin, S K Nayak, Emmanuel Jacques,  
K A Brylev, N G Naumov, Y Molard

► **To cite this version:**

F Camerel, F Kinloch, O Jeannin, M Robin, S K Nayak, et al.. Ionic columnar clustomesogens associations between anionic hexanuclear rhenium clusters and liquid crystalline triphenylene tethered imidazoliums. Dalton Transactions, 2018, 47 (32), pp.10884-10896. 10.1039/c8dt02201a . hal-01862457

**HAL Id: hal-01862457**

**<https://univ-rennes.hal.science/hal-01862457>**

Submitted on 14 Sep 2018

**HAL** is a multi-disciplinary open access archive for the deposit and dissemination of scientific research documents, whether they are published or not. The documents may come from teaching and research institutions in France or abroad, or from public or private research centers.

L'archive ouverte pluridisciplinaire **HAL**, est destinée au dépôt et à la diffusion de documents scientifiques de niveau recherche, publiés ou non, émanant des établissements d'enseignement et de recherche français ou étrangers, des laboratoires publics ou privés.

# Ionic Columnar Clustomesogens: Associations between Anionic Hexanuclear Rhenium Clusters and Liquid Crystalline Triphenylene Tethered Imidazoliums

F. Camerel,<sup>a,\*</sup> F. Kinloch,<sup>a</sup> O. Jeannin,<sup>a</sup> M. Robin,<sup>a,b</sup> S. K. Nayak,<sup>a</sup> E. Jacques,<sup>b</sup> K. A. Brylev,<sup>c</sup> N. G. Naumov,<sup>c</sup> Y. Molard<sup>a,\*</sup>

<sup>a</sup> Univ Rennes, CNRS, ISCR - UMR 6226, ScanMAT – UMS 2001, F-35000 Rennes, France; E-mail : franck.camerel@univ-rennes1.fr, yann.molard@univ-rennes1.fr.

SKN current address: Department of Chemistry, Visvesvaraya National Institute of Technology, Nagpur, Maharashtra-440010, India

<sup>b</sup> Univ Rennes, CNRS, IETR - UMR 6164, Département Microélectronique & Microcapteurs, F - 35000 Rennes, France.

<sup>c</sup> Nikolaev Institute of Inorganic Chemistry, Siberian Branch of the Russian Academy of Sciences, 3 Acad. Lavrentiev pr., 630090 Novosibirsk, Russia  
Novosibirsk State University, 2 Pirogova Str., 630090 Novosibirsk, Russia

Providing several functionalities to a single material is an emerging challenge with many industrial prospects in material sciences. Self-assembled organic-inorganic hybrid materials endowed with emission properties are part of these new materials. While the inorganic moieties provide emissivity, the organic part confers its nanostructuration and process-abilities. Here we describe how columnar arrangements can be obtained by assembling, via electrostatic interactions, isometric anionic inorganic nanoemitters, namely  $[\text{Re}_6\text{Se}_8\text{CN}_6]^{4-}$ , with imidazolium counter cations bearing triphenylene units. The resulting hybrids combine the emission of both components and energy transfer have been evidenced between both entities. Hole charge mobilities of the hybrid organic-inorganic columnar mesophases was also evaluated by the space charge limited current (SCLC) method.

## Introduction

Light emissive and conductive hybrid organic-inorganic materials turn out to be very promising for applications in lighting, optoelectronic or photovoltaism. They possess a good process-ability provided by their organic part while their inorganic counterpart offers a generally stable and intense emission. Yet, such materials show large scale and low-cost processing potentialities (dip- or spin-coating, drop casting, printing) compared to purely inorganic industrial solutions based on silicon.<sup>1-4</sup> Challenges exist still in this class of materials to avoid the self-aggregation of inorganic emitters in the organic matrix, but, more importantly, to control the structuration at the nanometer scale of the whole material. In this frame, liquid crystals (LC) possess all the necessary characteristics like fluidity, self-organization abilities, capacities to react to external stimuli and to control the nanostructuration of new functionalities in a single material.<sup>5</sup> The ionic self-assembly approach (ISA) is a powerful tool for the facile generation of highly organized phases from functional charged molecules and protomesogenic counter-ions. Liquid crystalline phases have been obtained by association of purely organic molecules with imidazolium or ammonium carrying long carbon chains.<sup>6-8</sup> This strategy was also applied to purely inorganic charged species<sup>9-13</sup> but also to metal complexes properly functionalized at the periphery by charged fragments.<sup>14, 15</sup> Recently, the ionic self-assembly of phosphorescent 8-hydroxyquinoline-5-sulfonato/platinum(II) anionic complex with lipophilic imidazoliums was also described to lead to a variety of soft nanomaterials displaying strong red-emission in the solid state.<sup>16</sup> However, in almost all cases, such advanced self-assembled nanostructures were produced using charged amphiphilic molecules carrying long alkyl chains. Ionic liquid crystalline associations of functional charged molecules with oppositely charged fragments directly carrying rod-like or disc-like mesogenic fragments remain scarce.

Ionic liquid crystals have been designed from the ionic association between poly(ammonium) dendrimers or polymers with cholesteryl-, cyanobiphenyl-, azo compound- p-terphenyl based carboxylates.<sup>17-21</sup> An ionic liquid crystalline phase was also produced from a terbium-substituted hetero-polyoxotungstate complex encapsulated by ammonium carrying rod-like mesogenic groups.<sup>22</sup> More recently, ionic clustomesogens, *i.e.* ionic liquid crystals containing hexanuclear transition metal clusters with switchable magnetic and luminescence properties were obtained from ammonium cations carrying rod-like cyanobiphenyl fragments.<sup>23-28</sup>

Hexanuclear transition metal cluster compounds contain inorganic units of general formula  $[M_6Q^i_8X^a_6]^n$  ( $M = Mo, W, \text{ or } Re$ ;  $Q = \text{chalcogen/halogen}$ ;  $X = \text{anionic or neutral ligand}$ ;  $i = \text{inner, } a = \text{apical}$ ). They are based on an octahedron of metal atoms linked by metal-metal bonds inscribed in a cube of  $\mu_3\text{-}Q^i$  ligands (see, for example, structure of  $[Re_6Se_8(CN)_6]^{4-}$  in **Scheme 1**), which is assembled by a high temperature solid state synthesis starting from the corresponding elements and simple salts. Complexes with 24 cluster valence electrons can be highly phosphorescent in the red-NIR area.<sup>29-35</sup> Because of their high potential in biology for ROS production, as nanoscintillators or contrast agents,<sup>36-38</sup> in optoelectronic<sup>39-41</sup> or lighting,<sup>42</sup> many efforts have been devoted these last years to counterpart their ceramic-like behaviour and integrate them in host matrices.<sup>43-54</sup> Hence, several strategies have been developed to solubilize the  $[M_6Q^i_8X^a_6]^n$  anionic units in organic media,<sup>55, 56</sup> or to integrate them directly in a polymeric or liquid crystalline organic host matrix<sup>23, 25, 49, 57, 58</sup> by replacing, *via* a metathesis reaction, their alkali counter cations by functional organic ones. Nonetheless, combining isometric transition metal clusters and rod-like mesogens through the ionic self-assembly approach leads only to nematic or lamellar liquid crystalline phases. And, to the best of our knowledge, no columnar phases could be isolated by this technic with such inorganic compounds. Luminescent columnar liquid crystals have attracted much interest in materials chemistry,<sup>59, 60</sup> in particular because they can display good unidimensional charge mobilities which are useful in the design of many devices including photovoltaic solar cells, field effect transistors, one dimensional conductors and light emitting diodes.<sup>61</sup> Recently, an original supramolecular strategy using discotic crown-ether able to complex the alkali counter cations of the anionic cluster units has been developed to design columnar liquid crystals.<sup>62</sup>

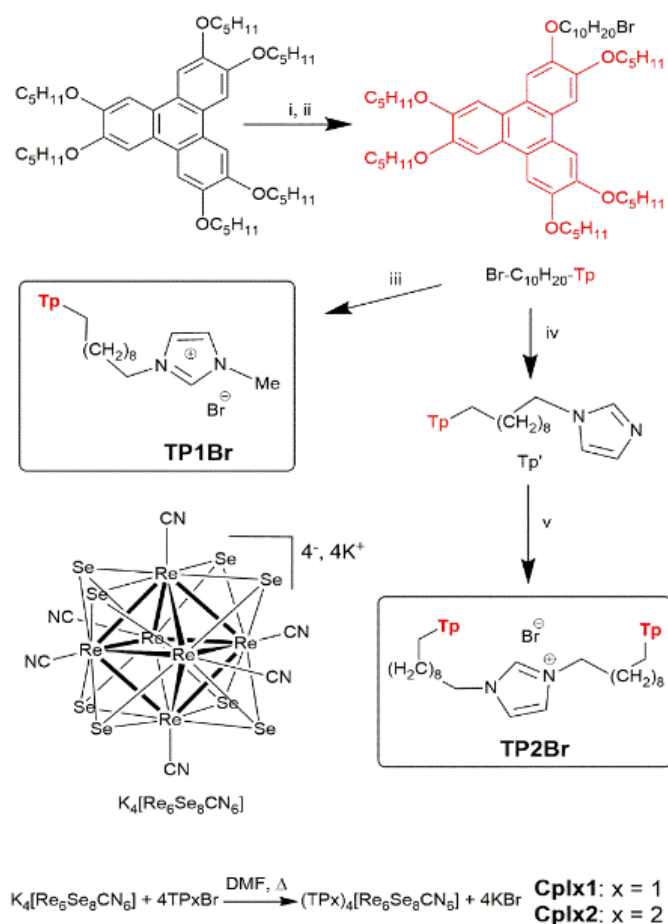
Triphenylene (TP) derivatives are archetypical of discotic liquid crystals (DLCs).<sup>59</sup> The large  $\pi$ -conjugated system with high symmetry can easily be functionalized and the grafting of linear alkyl chains from C4 to C11 allows the facile emergence of columnar mesophases of hexagonal symmetry ( $Col_h$ ). In addition, the columns formed through the stacking of the large aromatic triphenylene cores display excellent photoelectric properties.<sup>63, 64</sup> Here, we demonstrate that the ionic association of discotic liquid crystalline TP tethered imidazoliums to hexanuclear rhenium clusters allow the emergence of original crystalline and liquid crystalline columnar phases in which the spherical anions and the TP moieties can be packed into lamellae or columns. The red-NIR emissive  $[Re_6Se_8(CN)_6]^{4-}$  cluster anionic unit has been chosen for two main reasons: i) the high stability of the Re – CN bond towards potential ligand exchange and ii) its higher anionic charge compared to  $Mo_6$  or  $W_6$  anionic halide clusters. It allows a higher number of mesogenic units to surround the nanosized metallic cores that should favour fluidity and self-assembling abilities. The ionic hybrid combines the emission properties of each component and partial energy transfer was evidenced between them. Space charge limited current (SCLC) measurements have also been performed to evaluate the hole charge transportation abilities of the films.

from a dichloromethane/ $CH_3CN$  mixture. The 1:4 ratio as well as the purity of rhenium salts were confirmed by elemental analyses. EDX analyses confirmed the effectiveness of the ion exchange since no trace of potassium or bromine was detected. The efficiency of the metathesis was further confirmed by  $^1H$  NMR experiments. The signal corresponding to the imidazolium C(2)-proton undergoes a 1 ppm upfield shift upon exchange of the bromine anion by the anionic cluster complex. The hybrid salts could be dissolved in various organic solvents ( $CH_2Cl_2$ ,  $CHCl_3$ , THF, toluene...) and casted into large transparent and coloured films. In this way, two salts of hexanuclear anionic clusters with imidazolium ion-anchored triphenylene as counter-ions have been properly isolated: **(TP1)<sub>4</sub>[Re<sub>6</sub>Se<sub>8</sub>(CN)<sub>6</sub>]** and **(TP2)<sub>4</sub>[Re<sub>6</sub>Se<sub>8</sub>(CN)<sub>6</sub>]** denominated in the next sections **Cplx1** and **Cplx2**, respectively.

### Thermal and self-organizing properties.

The liquid crystalline properties of **TP1Br**, **TP2Br** and their respective complexes with the rhenium cluster anion were first investigated by differential scanning calorimetry (DSC) and polarized optical microscopy (POM), then by powder X-ray diffraction as detailed below. The transition temperatures and enthalpies of all compounds are gathered in **Table 1**. The DSC traces of **TP1Br** display one reversible first order transition centered at 105 °C (see ESI, **Figure S1**). Another endothermic signal is also observed at 55 °C on heating and is attributed to crystal to mesophase phase transition. On cooling, the reverse process (exothermic peak) is not observed, indicating that the crystallization is a slow process, extending over a broad temperature range. On cooling from the isotropic state, a homogeneous and fluid texture (developable cylindrical domains) characteristic of a columnar phase develops between crossed-polarizers, as expected with this kind of mesogens (see ESI, **Figure S2**).<sup>67-69</sup> Temperature-dependent XRD analyses confirm that the two transitions are located between 40 and 60 °C and between 100 and 120 °C on cooling and on heating (see ESI, **Figures S3-4**). X-ray diffraction patterns recorded at 120 °C displayed

only broad halos in the whole  $2\theta$  angular range ( $0.95^\circ \leq 2\theta \leq 31.6^\circ$ ), confirming that the compound is in an isotropic state at this temperature. Between 100 and 60 °C, the pattern exhibits a series of sharp peaks in the small angle region that can be indexed as the reflections of a rectangular lattice ( $a = 77.2 \text{ \AA}$ ,  $b = 68.9 \text{ \AA}$  at 100 °C). The peak at  $d = 17.05 \text{ \AA}$  does not fit with the rectangular indexing and shows a very strong intensity compared to the other peaks. This reflection can be attributed to the organization of the TP fragments in a 2D array of hexagonal symmetry. In fact, pure 2,3,6,7,10,11-hexakis(pentyloxy)triphenylene compound forms a columnar mesophase of hexagonal symmetry between 69 and 122 °C (see ESI, **Figure S5** for the SAXS pattern).<sup>70</sup> SAXS experiments performed at 90 °C on this compound confirm the formation of a hexagonal columnar mesophase with a lattice parameter  $a = 20.0 \text{ \AA}$  displaying a strong reflection at  $d = 17.32 \text{ \AA}$ . This organization was also confirmed by molecular dynamic calculations.<sup>71</sup> Thus, such SAXS pattern can be explained by a segregation of the imidazolium fragments into columns inside the hexagonal array of TP columns which in turn leads to the detection of a larger array of rectangular symmetry. The rectangular cell with the lattice parameters  $a = 77.2 \text{ \AA}$  and  $b = 68.9 \text{ \AA}$  perfectly fits in the hexagonal array of lattice parameter  $a = 19.7 \text{ \AA}$ . In the wide angle region, a broad halo centred at  $4.5 \text{ \AA}$ , associated to the mean distance between the alkyl chains in a molten state, confirms the liquid crystalline nature of the phase.



**Scheme 1.** Synthesis of the triphenylene-substituted imidazolium salts. Reagents and conditions: (i) *B*-Bromocatecholborane,  $\text{CH}_2\text{Cl}_2$ , r.t.; (ii) 1,10-dibromodecane,  $\text{K}_2\text{CO}_3$ , acetone,  $\text{N}_2$ , reflux; (iii) 1-methylimidazole, toluene, 120 °C,  $\text{N}_2$ ; (iv) Imidazole, KOH,  $\text{CH}_3\text{CN}$ , 90 °C,  $\text{N}_2$ ; (v) 3,6,7,10,11-pentakis(pentyloxy)triphenylene-2-ol, toluene, 120 °C,  $\text{N}_2$ .

**Table 1.** Thermal behavior and X-ray characterization of **TP1Br**, **TP2Br** and corresponding ionic associations with hexanuclear clusters.<sup>a)</sup>

	Transition temperatures °C ( $\Delta H$ in J.g <sup>-1</sup> )	$d_{\text{meas}}/\text{\AA}$	hk/hkl	Mesophase parameters measured at T
<b>TP1Br</b>	Cr 55(2.1) LC	51.4	11	Col <sub>r</sub> T = 100 °C a = 77.2 $\text{\AA}$ b = 68.9 $\text{\AA}$ $a_{\text{hex}} = 19.7 \text{\AA}$ S = 5320 $\text{\AA}^2$ $V_{\text{cell}} = 18600 \text{\AA}^3$ $V_{\text{m}} = 1490 \text{\AA}^3$ N = 12
	109(6.1) Iso	38.6	20	
	Iso 102(-6.1) LC	34.2	02	
		25.7	22	
		19.3	40	
		17.05	$d_{\text{hex}}$	
		14.2	34	
		12.85	44	
		11.7	54	
		4.45	$h_{\text{ch}}$	
		3.6	$h_{\text{stack}}$	
<b>TP2Br</b>	Cr 58(1.7) LC	49.9	10	Col <sub>0</sub> T = 70°C a = 50.4 $\text{\AA}$ c = 39.35 $\text{\AA}$ $\beta = 82.5^\circ$ $a_{\text{hex}} = 19.9 \text{\AA}$ S = 1970 $\text{\AA}^2$ $V_{\text{cell}} = 6895 \text{\AA}^3$ $V_{\text{m}} = 2950 \text{\AA}^3$ N = 2
	93(5.9) Iso	39.0	01	
	Iso 81(-6.0) LC	33.2	11	
		24.7	20	
		22.4	21	
		19.1	12	
		17.2	$d_{\text{hex}}$	
		16.5	22/30/31	
		14.4	32	
		13.0	13/03	
		11.8	23	
		11.25	42	
		4.4	$h_{\text{ch}}$	
	3.5	$h_{\text{stack}}$		
<b>Cplx1</b>	Cr 123(5.1) LC	51.4	001	Lam <sub>col</sub> T = 140 °C l = 51.4 $\text{\AA}$ $a_{\text{hex}} = 12.4 \text{\AA}$
	181(0.7) Iso	26.2	002	
	Iso 177(-0.7) LC	17.4	003	
	107(-5.2) Cr	13.1	004	
		10.75	10	
		6.2	11	
		4.0	$h_{\text{ch}}$	
<b>Cplx2</b>	Cr 77(1.4) LC	44.9	10	Col <sub>h</sub> T = 80 °C $a_{\text{hex}} = 51.8 \text{\AA}$
	101(0.3) Iso	25.6	11	
	Iso 85(-) LC 70(-0.8) Cr	22.2	20	
		16.8	21	
		11.0	001	
		5.6	002	
		3.5	$h_{\text{stack}}$	

<sup>a)</sup>  $d_{\text{meas}}$  are the measured diffraction peak spacings;  $I$  is the intensity of the reflection (VS: very strong, S: strong, M: medium, W: weak, VW: very weak), br and sh stand for broad and sharp reflections; hk is the indexation of the reflections corresponding to Col<sub>h</sub>, Col<sub>r</sub> and Col<sub>0</sub> phases, and 00l the indexation for the lamellar phase; The molecular volume  $V_{\text{M}}$  is determined by  $V_{\text{M}} = M/0.6022$ , where  $M$  is the molecular weight; Cr, crystalline phase; Iso, Isotropic liquid; Col<sub>h</sub>, hexagonal columnar mesophase; Col<sub>r</sub>, rectangular columnar mesophase; Col<sub>0</sub>, oblique columnar mesophase; Lam, lamellar phase;  $h_{\text{ch}}$ : maximum of the diffuse scattering due to lateral distances between molten aliphatic tails,  $h_{\text{stack}}$ : diffuse scattering due to  $\pi$ - $\pi$  stacking.  $S$  is the surface area of the unit cell.  $N$  is the number of molecule contained in a  $h_{\text{stack}}$ -thick unit cell and is directly deduced from the relation  $N = V_{\text{cell}}/V_{\text{m}}$  with  $V_{\text{cell}} = S \times h_{\text{stack}}$ .

An additional peak ( $h_{\text{stack}}$ ) centred at 3.6 Å is also observed and is attributed to the stacking distance between the TP fragments along the column axis. Upon temperature changes, the peak positions in the small angle region are weakly affected and only a slight increase of the stacking distance ( $h_{\text{stack}}$ ) is observed upon heating between 60 and 100 °C from 3.54 to 3.60 Å in the liquid crystalline phase. Below 40 °C, the compound is in a crystalline state, as revealed by the apparition of several sharp peaks in the wide angle region. To gain some insight into the packing of **TP1** inside the unit cell, a standard geometrical treatment was applied.<sup>72</sup> The unit cell volume ( $V_{\text{cell}}$ ) in a rectangular lattice is calculated as  $a \times b \times h_{\text{stack}}$ , where  $a$  and  $b$  are the lattice constants and  $h_{\text{stack}}$  is the mean stacking distance between the molecule deduced from the X-ray patterns (3.5 Å). The number of molecules inside the unit cell  $h_{\text{stack}}$ -thick is directly given by the relation  $N = V_{\text{cell}}/V_m$  in which  $V_m$  is the molecular volume estimated by  $V_m = (M_w/0.6022)$  assuming a reasonable value for the density of 1 g cm<sup>-3</sup>. Thus, dividing the unit-cell volume by the molecular volume, it was found that the rectangular unit cell  $h_{\text{stack}}$ -thick contained 12 **TP1Br** molecules. Based on the X-ray data and the number of molecules inserted inside the unit cell, a packing model is proposed in **Figure 1a**. The rectangular lattice contains 16 nodes of the underlying hexagonal lattice. If 12 TP cores are placed on the nodes of the hexagonal lattice, 4 nodes remains free to accommodate the imidazolium fragments, meaning that the ionic columns is constituted by three imidazolium fragments of three surrounding **TP1** cations. This is in good accordance with the difference between the volume fraction of an imidazolium fragment ( $V_{\text{arom}} = 135 \text{ \AA}^3$ ) and the one of a TP core ( $V_{\text{arom}} = 380 \text{ \AA}^3$ ). The **TP1** cation dimensions also perfectly fit in this array since the centroid-centroid distance between the imidazolium fragment and the TP aromatic core was evaluated by Dreiding model to ~20 Å. The bromide counter-ions are likely localized inside the ionic columns. The molecules have been placed to obtain a primitive lattice and to have six surrounding TP columns around each imidazolium columns.

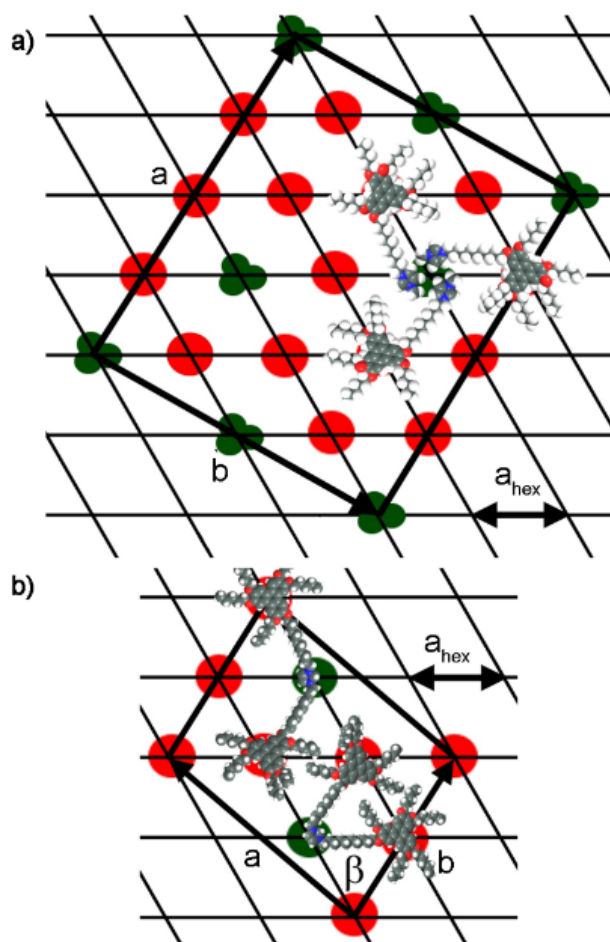


**Figure 1.** Proposed model for the organization of a) **TP1Br** and b) **TP2Br** in the liquid crystalline phase (green = imidazolium columns; red = triphenylene stacks).

TP carrying one pendant imidazolium fragment connected through a pentoxy chain<sup>73</sup> and TP-imidazolium-based ionic dimers<sup>74</sup> have already been reported to form a columnar mesophase but the true molecular organization and the microsegregation between the aromatic and the ionic parts have never been properly elucidated. Only very

recently, microsegregation processes occurring with some pentadodecyloxytriphenylene-imidazolium salts and their NHC metal complexes have been elucidated inside columnar mesophases of rectangular symmetry.<sup>75</sup> TP carrying six pendant imidazolium fragments have also been reported to form ionic liquid crystalline materials of cubic or hexagonal symmetries but they can be more simply described as a dispersion of TP columns inside continuum of alkyl-imidazolium fragments acting as an ionic liquid.<sup>76, 77</sup>

The DSC traces of **TP2Br** (see ESI, **Figure S6**) strongly resemble the ones of **TP1Br** but with a reduced LC domain. The high temperature transition at 93 °C was unambiguously attributed by POM to the liquid crystal to isotropic phase transition (see ESI, **Figure S7**). Cooling from the isotropic liquid, a fluid and birefringent texture with pseudo-fan shapes, typical of a columnar phase, is observed. Temperature-dependent XRD analyses confirm that at low temperatures, the compound is crystalline and several sharp peaks are observed in the entire range of explored  $2\theta$ . Between 52 and 93 °C on heating or 82 and 30 °C on cooling, the compound is in a liquid crystalline state, as revealed by the presence of several sharp peaks in the low angle region together with a broad halo ( $h_{ch}$ ) in the wide angle region which indicates that the alkyl chains are in a molten state (see ESI, **Figure S8**). An additional peak ( $h_{stack}$ ) centred at 3.5 Å, coming from the stacking of the TP fragments, is also observed. The sharp peaks observed in the small angle region can be indexed in 2D array of oblique symmetry with  $a = 50.4$  Å,  $c = 39.35$  Å and  $\beta = 82.5^\circ$  at 70 °C. As for **TP1Br**, an intense peak at  $d = 17.21$  Å, which cannot be indexed, was also observed and was attributed to the fundamental diffraction line of a 2D hexagonal lattice of the TP columns. The formation of an oblique lattice together with a hexagonal sub-lattice, point to a segregation of the imidazolium fragments into columns inside the hexagonal columnar mesophase of TP columns. The oblique lattice was found to perfectly fit into a hexagonal array with a lattice parameter of 19.9 Å. Using the standard geometrical treatment applied for **TP1** cation, the unit cell volume of the oblique lattice  $h_{stack}$ -thick was calculated and the molecular volume was estimated, it was found that 2 **TP2** cations fill the unit cell. The oblique cell contains 6 nodes of the underlying hexagonal array. This implies that only one imidazolium fragment is localized in each ionic columnar stratum. Based on all these observations, a packing model is proposed in **Figure 1b**. The cell lattice parameters are also here in accordance with the molecular dimensions and in this model two possible molecular configurations should be taken into account. Such materials with ionic columns and  $\pi$  stacks can be of great interests to develop dual electronic and ionic conductors.<sup>78</sup>

DSC analysis of **Cplx1** compound revealed that this material undergoes a marked first order transition centered at 115 °C and second very weak first order transition at 178 °C (see ESI, **Figure S9**). POM observations showed that above the first transition, the solid compound melts into a birefringent gel up to the high temperature transition, above which the compound is an isotropic liquid. The observation of a fluid and birefringent material between 115 and 178 °C is a good indication of a liquid crystalline phase formation. In addition, the observation of a POM texture displaying pseudo-fan shapes upon cooling from the isotropic melt points to the formation of a columnar mesophase (see ESI, **Figure S10**).

Temperature-dependent SAXS measurements confirm the formation of a LC phase between 115 and 178 °C. Above 180 °C, the SAXS patterns displays several broad peaks, corresponding to the mean distances of the various constituting parts in a molten state. All the recorded XRD diffractograms (between 120 to 160 °C) are identical and contain four sharp and intense small-angle reflections with reciprocal spacings in the ratios 1:2:3:4 (see ESI, **Figure S11**). These small-angle peaks are most readily assigned as the (001), (002), (003) and (004) reflections of a lamellar phase with an interlayer spacing parameter  $a = 51.4$  Å (at  $T = 140$  °C, **Table 1**). The interlayer spacing linearly increases with the temperature decrease (from 50.8 Å at 160 °C to 52.05 Å at 120 °C). The SAXS patterns also display two additional broad reflections in the middle angle region with reciprocal spacings in the ratio  $1:\sqrt{3}$ , characteristic of a 2D array of hexagonal symmetry. This calculated hexagonal lattice parameter of  $a_{hex} = 12.4$  Å, insensitive to temperature changes, is too small to be associated to the TP fragments organization (triphenylene-triphenylene distance  $\sim 20$  Å). Thus, these two reflections are more likely associated to a 2D hexagonal organization of the cluster cores (cluster diameter  $\sim 12$  Å).<sup>24, 25</sup> In regard to the columnar phase POM texture, a model can be proposed in which the TPs are stacked into columns and these columns are then organized into layers with the imidazolium fragments pointing above and below the lamellas. The clusters are sandwiched between the TP layers and are organized in a compact 2D hexagonal array. The proposed model is depicted in **Figure 2**. In this model, the interlayer distance is also in accordance with the molecular dimensions. The imidazolium-TP distance was evaluated to be around 20 Å by Dreiding models and the cluster diameter is close to 12 Å. Thus, the interlayer spacing of  $\sim 50$  Å fits well with twice the imidazolium-TP distance plus the cluster diameter ( $2 \times 20 + 12$ ) as proposed in the model. To account for the cluster anion cross-section value and to produce a reasonable packing density in the alkyl chain sublayers, the polymethylene spacers should be conformationally disordered (in molten state as expected in the LC phase) and not all in an anti-conformation, in line with the presence of a broad halo at 4.0 Å. In the crystalline phase, the molecular organization observed in the LC phase is preserved but the SAXS patterns display several additional sharp peaks in the middle and wide angle regions indicative of the compound crystallization.

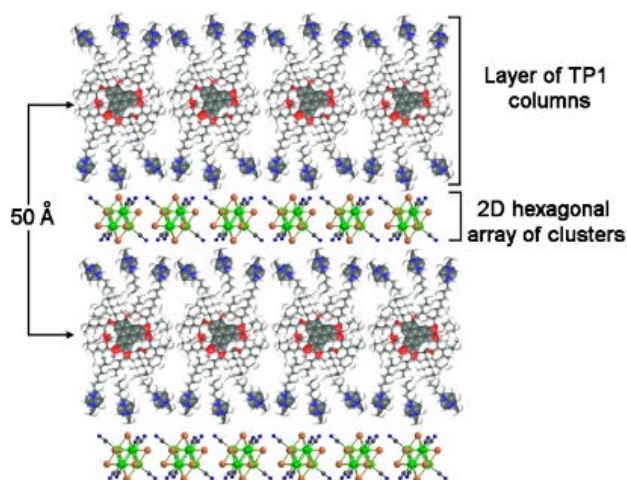


**Figure 2.** Proposed organization for **Cplx1** in the LC phase.

The DSC traces of **Cplx2** show two broad and weakly energetic thermal transitions at 77.4 and 101.2 °C on heating. The high temperature transition presents strong supercooling with an exothermic peak at 85 °C whereas the low temperature transition presents a rather small supercooling with an exothermic peak at 69.7°C (see ESI, **Figure S12**). The low-temperature transition is attributed to a crystal-to-mesophase transition whereas the high-temperature transition corresponds to the mesophase-to-isotropic liquid transition. Above 102 °C, the compound is in an isotropic fluid state (see ESI, **Figure S13**). Upon cooling, POM observations show that below 85 °C, the compound slowly forms a birefringent phase with an uncharacteristic texture of small defects. Shearing easily converts the texture into an unspecific, homogeneous fluid birefringent texture, which unambiguously indicates the liquid-crystalline nature of the material. Below 69°C, crystallization of the compound into a highly viscous and hardly deformable material is associated to a decrease of the birefringence intensity. To determine the nature of the mesophase, temperature-dependent SAXS experiments were performed. All the recorded XRD diffractograms in the mesophase temperature range are identical, and four sharp and intense small-angle reflections with reciprocal spacings in the ratios  $1:\sqrt{3}:\sqrt{4}:\sqrt{7}$  (see ESI, **Figure S14**), can be directly assigned as the (10), (11), (20) and (21) reflections of a hexagonal 2D lattice with a parameter  $a = 51.8 \text{ \AA}$  (at  $T = 80 \text{ }^\circ\text{C}$ , Table 1). Two lattice with a parameter  $a = 51.8 \text{ \AA}$  (at  $T = 80 \text{ }^\circ\text{C}$ , Table 1). Two broad reflections are also observed at 11.0 and 5.6 Å and are attributed in regard to the molecular dimension of the cluster to the 001 and 002 reflections coming from a 1D-stacking of the inorganic anions. Another broad diffraction peak is observed at 3.5 Å and is likely attributed to a  $\pi$ - $\pi$  stacking of the TP fragments into columns. In regard to the SAXS data and the molecular dimensions of the constituting parts, a model can be proposed in which 1-D chains of inorganic clusters surrounded by stacks of TP fragments are organized in an 2D-hexagonal array (**Figure 3**). To compensate the size and the charge of the cluster, it can be envisaged that two stacked pairs of **TP2** cations are contained inside the unit cell. In this model, the alkyl chains are in a fully extended configuration but of course, in the LC phase, these chains are in a molten state which should allow a better organization of columns and filling of the space. At low temperature, the main molecular organization is preserved but the SAXS patterns display some additional sharp peaks in the middle and wide angle regions, in line with the crystallization of the compound.

Lamello-columnar packings have already been reported for polypyridines,<sup>79</sup> metallomesogens,<sup>80</sup> donor-acceptor triads,<sup>81</sup> side-chain LC polymers,<sup>82</sup> or triazines with pendant TPs.<sup>83</sup> This type of organization is the easiest way to accommodate non-discotic fragments inside a phase containing columnar stacks of disk-like molecules. Thus, the observation of such organization with spherical clusters associated with discotic molecules could have been anticipated as in the case of **Cplx1**. Interestingly, the introduction of sterical constraint through the connection of two discotic fragments on one imidazolium head has led to an original columnar phase of hexagonal symmetry in which 1-D stacks of hexanuclear clusters are surrounded by stacks of triphenylene fragments. Such columnar organization of hexanuclear clusters remains scarce and has only been observed up to now in ternary polyionic

inorganic compound  $\text{Cs}_2\text{Mo}_6\text{Br}_{14}$  and 18-crown-6 ethers bearing two o-terphenyl units.<sup>62</sup> In addition, the association of emissive clusters with conducting stacking stacks of TP should be of great interest for applications in optoelectronic.

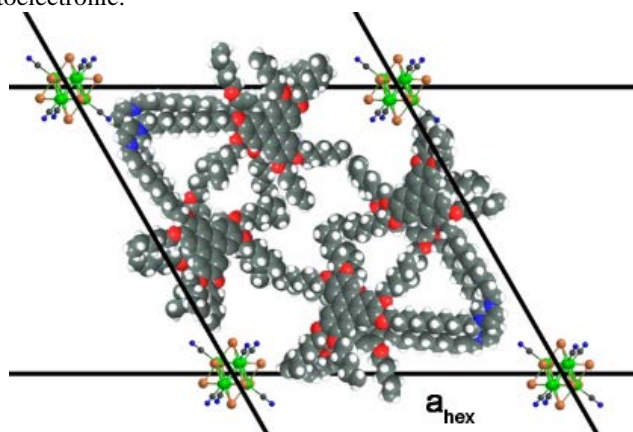
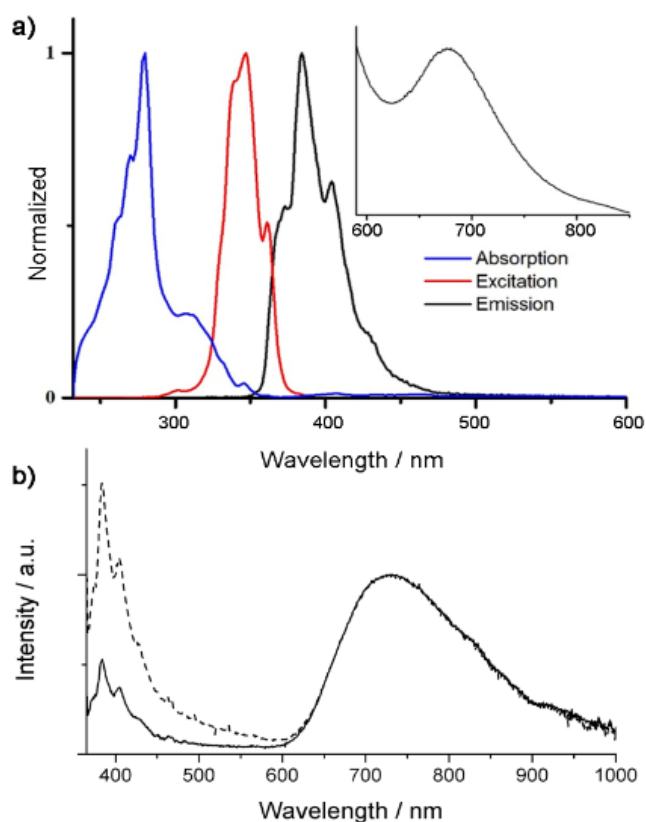


Figure 3. Proposed organization for **Cplx2** in the LC phase.

### Photophysical properties in solution.

The photophysical properties of **TP1Br**, **TP2Br** and corresponding complexes with  $[\text{Re}_6\text{Se}_8(\text{CN})_6]^{4-}$  clusters were first investigated in dichloromethane solution. All data are gathered in **Table 2**. The absorption spectra (see ESI, **Figure S15**) of **TP1Br** and **TP2Br** precursors display two main absorption maxima ( $\lambda_{\text{abs}}$ ) at 280 and 310 nm which are assigned to the  $\pi$ - $\pi^*$  and  $n$ - $\pi^*$  transitions from the TP fragments, respectively.<sup>84</sup> As expected, the absorption measured for **TP2Br** is twice the one measured for **TP1Br**. Due to the high absorption coefficient of the TP cores and the low one of the cluster core in the same area, absorption spectra of **Cplx1** and **Cplx2** are similar to the absorption spectra of **TP1Br** and **TP2Br**. Indeed, the absorption spectrum of the  $[\text{Re}_6\text{Se}_8(\text{CN})_6]^{4-}$  cluster core is composed by multiple bands in the range 210-550 nm with molar extinction coefficient below  $200 \text{ mmol}^{-1} \cdot \text{dm}^3 \cdot \text{cm}^{-1}$  corresponding to inner and apical ligand to metal charge transfers.<sup>23, 85</sup> The molar extinction coefficient of the hybrid main absorption band is four time higher compared to the one of the corresponding **TPi** ( $i = 1, 2$ ) which is in line with the expected stoichiometry between the TP fragments and the cluster. Emission spectra in solution were first recorded by exciting the compounds at their absorption maxima in aerated dichloromethane ( $c \sim 10^{-6} \text{ M}$ ). The emission spectra of **TP1Br**, **TP2Br**, **Cplx1** and **Cplx2** were found to be identical upon excitation at 280 nm or 310 nm with emission maxima ( $\lambda_{\text{em}}$ ) at 373, 384 and 404 nm (**Figure 4a** and see ESI, **Figure S16**). At this stage, several observations can be made: i) the formation of an excimer resulting from interactions between two TP units is not evidenced at this low concentration by steady state experiments at such excitation wavelength. The large Stokes' red-shift of 104 nm observed for all the compounds indicates large reorganization of the excited state, as also confirmed by the large red-shift (67 nm) of the excitation spectrum. ii) As **Cplx1** and **Cplx2** emission spectra are identical to TP spectra despite the presence of the anionic cluster core, which absorption bands are superimposed to the TP emission bands, only a partial energy transfer, if there is one, can be envisioned between the two emissive species in solution. No antenna effect are observed as it was the case when polyaromatic entities such as anthracene or pyrene were covalently attached to a  $\text{Mo}_6$  cluster core.<sup>86</sup> In fact, the bright red luminescence of the  $\text{Re}_6$  clusters (maximum at 710 nm, inset figure 4a) was hardly detectable and an overall absolute quantum yield (AQY) of 0.02 was estimated exciting samples at 370 nm. This low value is largely explained by the known ability of  $\text{Re}_6$  clusters excited triplet state to be quenched by molecular oxygen.<sup>32</sup>

Thus, emission properties were also investigated in deaerated solutions by bubbling  $\text{N}_2$  during 20 min in the cuvette prior measurements. **Figure 4b** presents obtained spectra for an excitation at 365 nm. Emission profiles of **Cplx1** and **Cplx2** were normalized to the cluster emission for comparison purposes. The emission of both TP units and cluster are clearly observed confirming that the TP energy is not, or not completely, transferred to the metal cluster. As expected, emission intensity of the TP part is higher for **Cplx2** than for **Cplx1** as compared to the cluster emission intensity. AQY of 0.1 and 0.07 were determined for **Cplx1** and **Cplx2**, respectively. Such luminescence allowed us to investigate lifetime of the excited state species by exciting samples in solution at  $C \approx 5 \cdot 10^{-4} \text{ mol L}^{-1}$ , at 375 nm with a pulsed laser diode and a streak camera. Two regions of the emission spectra were investigated: the TP emission window (380-640 nm) in fluorescence mode and the cluster emission window (640-780 nm) in phosphorescence mode (see ESI **Figure S19-24** for emission decays). Recorded data were corrected for fluorescence time frame to take into account the electronic response of the experimental set-up.



**Figure 4.** a) Absorption, excitation ( $\lambda_{\text{obs}} = 384$  nm) and emission spectra ( $\lambda_{\text{exc}} = 310$  nm) of **Cplx1** in aerated dichloromethane solution (insert: enlargement of the emission spectrum between 600 and 800 nm); b) Emission spectra of **Cplx1** (plain line) and **Cplx2** (dashed line) in deaerated dichloromethane ( $\lambda_{\text{exc}} = 365$  nm).

Calculated kinetic parameters are gathered in **Table 2**. Emission decays were fitted to one-, two- or three-exponential decay and the goodness-of-fit judged by the  $\chi^2$  values and the residual distribution. **TP1Br** and **TP2Br** emission decay profiles were integrated from 390 up to 500 nm and could be fitted with two components in the nanosecond range. Calculated values are in the range of reported values for TP derivatives functionalized with hexyloxy alkyl chains (a value of 7 ns was reported by Markovitsi *et al.*<sup>87, 88</sup> while Miguel-Coello *et al.*<sup>75</sup> described an emission lifetime value lying around 9 ns). Usually TP derivatives show a monoexponential behavior in diluted solutions. The presence of a second component, beside the presence of an emitting impurity, might be interpreted as the result of interactions between the imidazolium head and the TP units,<sup>89</sup> but more preferably, by analogy with already reported intramolecular excimer forming polycyclic systems,<sup>90-92</sup> to the existence of a weakly emissive excimer. In this last case, the shorter decay (2.5 ns - 3.4 ns) is attributed to the emission of the locally excited TP (monomer emission) while the longest one (5.6 ns - 7.6 ns) is due to the excimer. Let us stress that in previous studies, TP derivatives were excited at much shorter wavelength than in our case. In particular, Markovitsi *et al.*<sup>93, 94</sup> used a 266 or 344 nm excitation; more recently, Miguel-Cuello *et al.*<sup>75</sup> worked with a 320 nm beam, and, Ikeda *et al.*,<sup>95</sup> who were the first to report the TP excimer emission, used a 350 nm excitation source. We therefore investigated how the excitation wavelength was influencing the TP emission abilities in their low absorption window between 320 nm and 380 nm. **Figure 5** shows the emission spectra obtained for **TP1Br** and **TP2Br** at 320

nm, 350 nm and 375 nm (see ESI **Figure S17-S18** for emission spectra with intermediate excitation wavelength). It is clear from these spectra that an emission signal centered around 525 nm and corresponding to the excimer emission<sup>95</sup> appears at low wavelength excitation, which is in good agreement with our calculated emission decay fits. The phenomenon is more pronounced for **TP2Br**, as shown by spectra obtained for a 350 nm excitation. This excimer becomes poorly emissive when TP units are associated to the cluster core, as its emission is not detected in the emission spectra of **Cplx1** and **Cplx2** (**Figure 4**). Thus, the presence of a third component in the emission decay of complexes when looking at the TP emission window in fluorescence mode indicates that some energy transfer occurs in solution between TP moieties and the cluster cores. This transfer is also illustrated in phosphorescence mode for **Cplx2** by the presence of two components in the emission decay. Note that Markovitsi *et al.*<sup>93</sup> reported, for a TP unit hexafunctionalized by hexylkoxy chains, a delayed fluorescence emission lifetime value of 0.49  $\mu\text{s}$  at 20°C, value close from the one calculated for the short component of **Cplx2** (0.44  $\mu\text{s}$ ). In phosphorescence mode, kinetic parameters calculated for the cluster emission window in **Cplx1** and **Cplx2** are in good agreement with already reported data for the photoluminescence of the  $[\text{Re}_6\text{Se}_8(\text{CN})_6]^{4-}$  anion in deaerated organic solvents, with an emission decay value lying around 13-14  $\mu\text{s}$ .<sup>32, 96</sup>

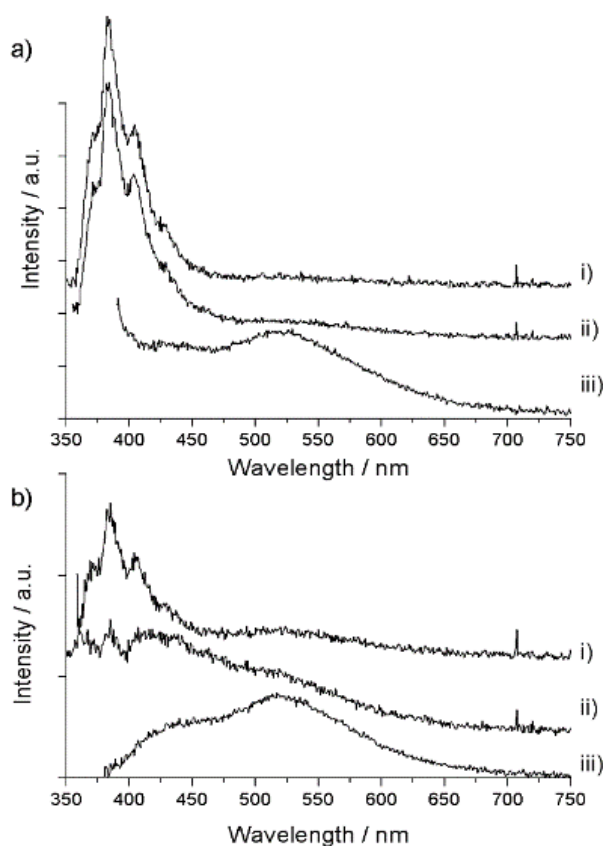


**Figure 5.** Emission spectra of a) **TP1Br** and b) **TP2Br** observed for excitation at i) 320 nm, ii) 350 nm and iii) 375 nm, in deaerated dichloromethane ( $C = 5 \cdot 10^{-4} \text{ mol L}^{-1}$ )

Table 2. Optical data and kinetic parameters measured in solutions and on powders at 298 K.

	$\lambda_{\text{abs}}$ (nm)	$\epsilon$ L.mmol <sup>-1</sup> cm <sup>-1</sup>	$\lambda_{\text{em}}$ solution (nm)	$\lambda_{\text{em}}$ film (nm)	$\Phi_{\square\square}$ (%)		Kinetic parameters <sup>a</sup>				
							Film	Solution	Film		
											380-510 nm
<b>TP1Br</b>	280 310	89.8 21.7	373 383 404	435 500	2.1	9.5	0.4 ns (0.77) 1.9 ns (0.17) 8.3 ns (0.06)	0.56 $\mu$ s (0.79) 2.13 $\mu$ s (0.21)	-	3.4 ns (0.58) 7.2 ns (0.42)	-
<b>TP2Br</b>	280 310	198 59.8	373 384 404	445 500	1.4	9.4	2.8 ns (0.42) 7.9 ns (0.58)	0.53 $\mu$ s (0.81) 2.16 $\mu$ s (0.19)	-	2.5 ns (0.60) 5.6 ns (0.40)	-
<b>Cplx1</b>	280 310	355.2 102.9	372 385 404	710	5.2	10 <sup>b</sup> /2.3 <sup>c</sup>	0.5 ns (0.61) 4.1 ns (0.20) 9.1 ns (0.19)	0.11 $\mu$ s (0.73) 0.66 $\mu$ s (0.17) 2.67 $\mu$ s (0.10)	2.58 $\mu$ s (0.47) 7.55 $\mu$ s (0.53)	0.9 ns (0.53) 2.8 ns (0.32) 7.0 ns (0.16)	13.8 $\mu$ s
<b>Cplx2</b>	280 310	808.3 203.4	371 384 403	525 710	7.0	7.4 <sup>b</sup> /2.0 <sup>c</sup>	0.7 ns (0.82) 2.9 ns (0.15) 10.2 ns(0.03)	0.09 $\mu$ s <sup>d</sup> 2.2 $\mu$ s <sup>d</sup>	3.70 $\mu$ s (0.54) 8.22 $\mu$ s (0.46)	0.8 ns (0.40) 3.4 ns (0.43) 7.6 ns (0.18)	13.6 $\mu$ s (0.01) 0.44 $\mu$ s (0.99)

<sup>a</sup> Normalized statistical weight are indicated in parenthesis; <sup>b</sup> in deaerated solution; <sup>c</sup> in aerated solution; <sup>d</sup> Integrating signal on the full profile gives a statistical weight of 99.993 % for the shortest component.

### Photophysical properties in the solid state.

The solid-state emission spectra were also recorded on the pristine powders thanks to a microscope equipped with a spectrometer and the absolute quantum yields were determined using an integrating sphere. The emission spectra are presented in **Figure 6c** and the luminescence data in solid state are also gathered in **Table 2**. Thin films of **TP1Br** and **TP2Br** showed a blue luminescence when irradiated with UV light at 340-380 nm. The emission spectra of **TP1Br** and **TP2Br** display a broad emission band centred at 500 nm. The shift of 115 nm observed to longer wavelength between the solid-state and the solution indicates an increase of the intramolecular interactions between the TP fragments in the condensed matter. A similar red-shift is typically observed in liquid crystalline phases and in gels of TP derivatives due to a stabilization effect of the excited state in the stacked aggregates.<sup>95</sup> These results indicate a conventional staggered overlap between the TP cores as usually found in LC phase and is related to the excimer formation. Thin films of **Cplx1** and **Cplx2** show a bright red luminescence when irradiated

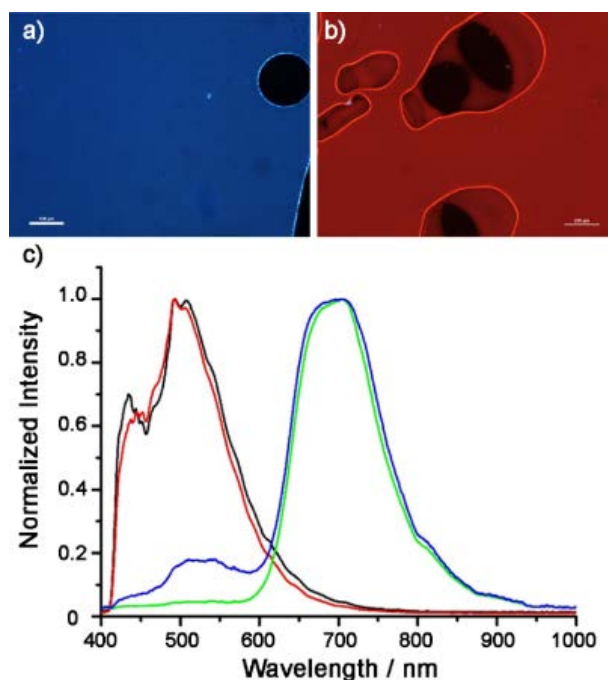


**Figure 6.** Pictures of a) **TP1Br** and b) **Cplx1** under UV excitation; c) solid state emission spectra of **TP1Br** (black), **TP2Br** (red), **Cplx1** (green) and **Cplx2** (blue) ( $\lambda_{exc} = 350-380$  nm)

with UV light at 340-380 nm. The emission spectrum of **Cplx1** displays only a broad emission band centered at 710 nm extending from 600 to 950 nm (**Figure 6c**). This red emission is attributed to the cluster core. The emission

from the TP fragments is nearly extinguished, indicating an efficient through-space energy transfer from the TP fragment to the  $\text{Re}_6$  cluster. This behavior can be attributed to FRET (Förster Resonance Energy Transfer) mechanism with the TP fragments acting as the donor and the cluster core as the acceptor. This assumption is first supported by the excitation profile corresponding to the cluster core (350-540 nm) which overlaps the TP emission band (400-700 nm). It should be noticed that this red-luminescence remains at high temperature (up to 150 °C). The emission spectrum of **Cplx2** also displays a broad and intense emission band in the red region attributed to the  $\{\text{Re}_6\text{Se}_8\}^{2+}$  cluster core but a weak and broad emission band centered at 510 nm is also visible. This high energy band is attributed to some residual emission coming from the TP fragments. In fact, in the case of **Cplx2**, a higher number TP fragments are surrounding the cluster core (8 per complex) and the cluster core cannot totally absorb/convert the energy coming from all the donors. The solid-state absolute quantum yields of the TP precursors

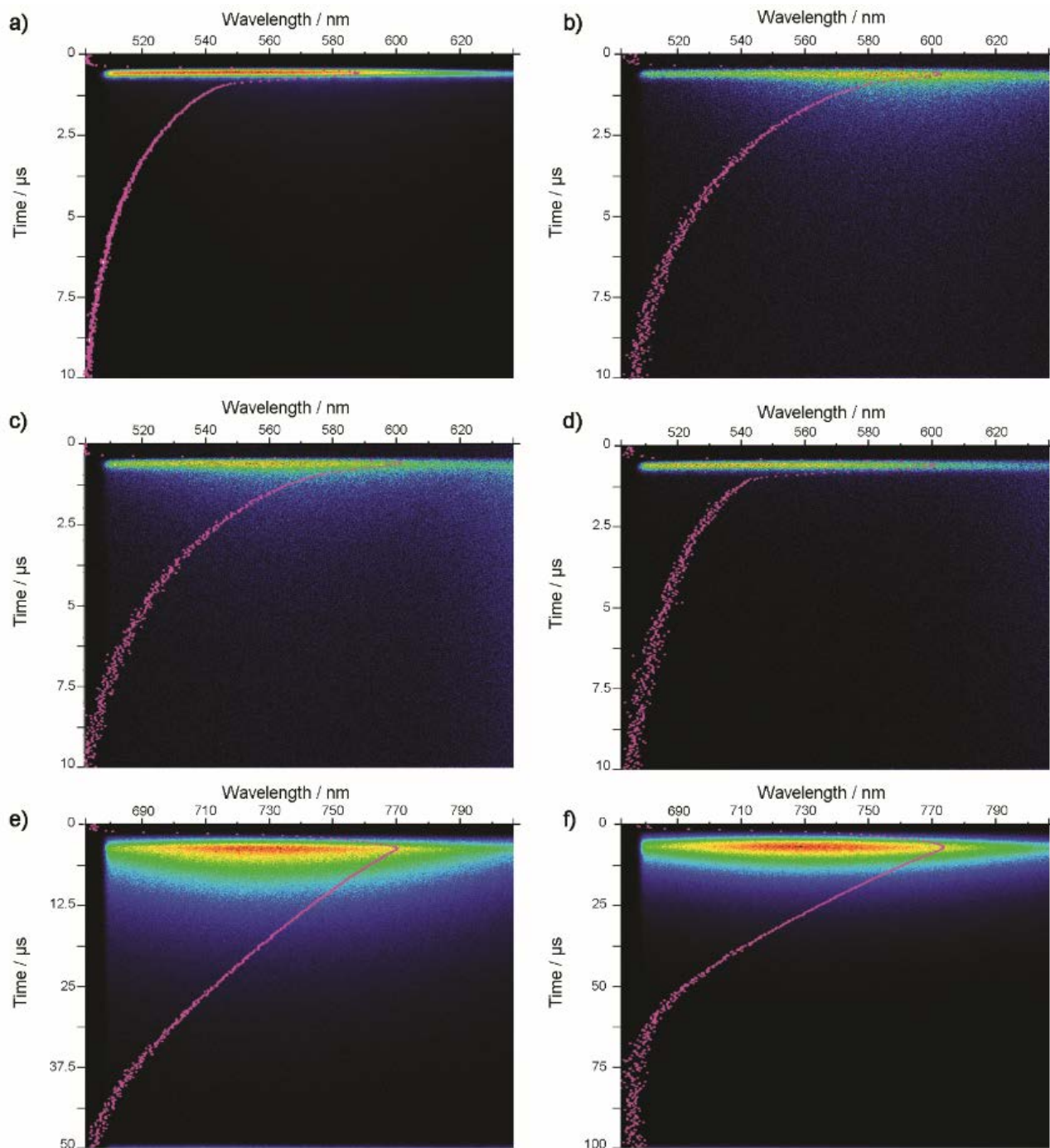


**Figure 7.** Solid state emission maps and integrated profiles in phosphorescence mode for a) **TP1Br**, b) **TP2Br**, c) and e) **Cplx1**, d) and f) **Cplx2**. Emission intensity increases passing from black-blue-green-yellow to red colour.

**TP1Br** and **TP2Br** were found to be around 2 % whereas the ones of **Cplx1** and **Cplx2** were found to be around 5-7 %.

Time dependent emission profiles were recorded for all samples at 23°C to get more insight about intramolecular interactions occurring between the TP units and the cluster core. Three wavelength windows were examined with different time scales (*e.g.* fluorescence or phosphorescence mode) to observe the evolution of i) the fluorescence of TP units on the monomer and excimer emission, ii) the known delayed fluorescence and phosphorescence of TP units<sup>93</sup> and iii) the phosphorescence of cluster cores. For **TP1Br** and **TP2Br**, emission profiles were recorded between 390 and 520 nm and could only be fitted with a complicated three exponential decay. However, one can notice that the excimer emission component (8.3 ns – 10.2 ns) increases from the liquid to the solid state as a result of a decrease of the compound mobility inducing a decrease of the non-radiative transition.<sup>93</sup> The same phenomenon is observed when the cluster cores replace the bromine counter cations. In Phosphorescence mode on the 510–630 nm emission window (**Figures 7a-7d**), the delayed fluorescence (lifetime of 0.5-0.6 μs) and phosphorescence (lifetime value of 2.13-2.67 μs) of TP moieties could be detected for **TP1Br**, **TP2Br** and **Cplx1**. Surprisingly, for **Cplx2**, the delayed fluorescence component is not detected while the phosphorescence component (2.2 μs) has a very low statistical weight compared to the component of 0.09 μs. This is very well illustrated in **Figure 7d** by the shape of the integrated emission decay profile. The second lifetime component observed in the cluster emission window could originate from the energy transfer between the triplet state of TP units and the emissive triplet state of Re<sub>6</sub> clusters. Such measurements confirm that, although TP units are not covalently connected to the cluster core, they are able to transfer part of their energy, presumably through a Forster mechanism, to the metallic cluster core.

### Charge mobility measurements.

Electrical measurements were carried out on Au/OSC/Au diode with coplanar configuration (see ESI). In a first attempt, we tried to determine the hole carrier mobilities of **TP1Br** and **TP2Br** using space-charge-limited current (SCLC) measurements. Unfortunately, the current densities were not high enough to reach the trap-free region of the SCLC regime, required to extract mobilities. Similar results were obtained with **Cplx1** and **Cplx2**. In fact, replacing the native bromine counter anion of **TP1** or **TP2** with the anionic cluster induces a decrease of the layer conductivity by one order of magnitude (**TP1(or TP2)-Br**:  $2.5 \cdot 10^{-10} \Omega^{-1} \text{cm}^{-1}$  / **Cplx1** or **Cplx2**:  $2 \cdot 10^{-11} \Omega^{-1} \text{cm}^{-1}$ ). SCLC measurements strongly depend on the thermal history of the samples and their alignments, but no change on the charge mobility values was observed after thermal annealing.

## Conclusions

The ionic association of hexanuclear anionic [Re<sub>6</sub>Se<sub>8</sub>(CN)<sub>6</sub>]<sup>4-</sup> clusters with imidazolium ion-anchored triphenylene leads to an original series of functional complexes displaying mesomorphic and red-phosphorescent properties. The hybrid combining a [Re<sub>6</sub>Se<sub>8</sub>(CN)<sub>6</sub>]<sup>4-</sup> cluster with TP monosubstituted imidazolium cations forms a lamello-columnar mesophase stable over a large temperature range. In this mesophase, the clusters are confined into 2D hexagonal arrays between layers of TP columns. Increasing the number of TP fragments by cation metathesis with TP disubstituted imidazolium cation leads to the formation of a columnar mesophase of hexagonal symmetry made of columns of clusters and columns of TP fragments. Such molecular organization is usually hard to achieve with spherical bulky anions. We succeeded in this work by combining a discotic molecule having a strong tendency to form columnar phases to spherical clusters. The molecular organizations of the newly developed imidazolium ion-anchored TP with bromide as counter-ion were also elucidated inside the mesophases, revealing a high degree of complexity with such multicomponent molecules. Photophysical studies showed that it is possible to observe the excimer emission of TP fragments by irradiating **TP1Br** or **TP2Br** in their low absorption window in solution and in the solid state. If this excimer is not detected by steady state measurements for **Cplx1** and **Cplx2**, its formation could be evidenced by time dependent emission studies. Even though the organic and inorganic emitters are not covalently connected, they are able to communicate in the solid state as well as in solution. In the solid-state, a strong red-luminescence originating for the cluster anions can easily be detected and an efficient energy transfer from the TP cores to the inorganic emitters is observed. Unfortunately, good electrical conduction pathways could not be obtained inside thin films at room temperature which implies that new routes should be discovered to properly align these columnar phases at the macroscopic scale.

## Acknowledgements

This work was supported by the University of Rennes 1, the CNRS, Rennes Metropole, ANR Clustomesogen ANR-13-BS07-0003-01, a Marie Curie International Incoming Fellowship within the 7th European Community Framework Program, the LIA Cluspom and grant RFBR 17-53-16015.

## References

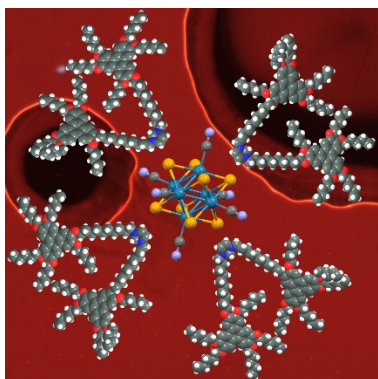
1. W. U. Huynh, J. J. Dittmer and A. P. Alivisatos, *Science*, 2002, **295**, 2425-2427.

2. F. Meinardi, H. McDaniel, F. Carulli, A. Colombo, K. A. Velizhanin, N. S. Makarov, R. Simonutti, V. I. Klimov and S. Brovelli, *Nat. Nanotechnol.*, 2015, **10**, 878-885.
3. S. Masi, S. Colella, A. Listorti, V. Roiati, A. Liscio, V. Palermo, A. Rizzo and G. Gigli, *Sci. Rep.*, 2015, **5**, 7725.
4. S. Parola, B. Julián-López, L. D. Carlos and C. Sanchez, *Adv. Funct. Mater.*, 2016, **26**, 6506-6544.
5. T. Kato, J. Uchida, T. Ichikawa and T. Sakamoto, *Angew. Chem. Int. Ed.*, 2018, doi: 10.1002/anie.201711163.
6. C. F. J. Faul and M. Antonietti, *Adv. Mater.*, 2003, **15**, 673-683.
7. C. F. J. Faul, *Mol. Cryst. Liquid Cryst.*, 2006, **450**, 255-265.
8. C. F. J. Faul, *Acc. Chem. Res.*, 2014, **47**, 3428-3438.
9. M. J. MacLachlan, N. Coombs and G. A. Ozin, *Nature*, 1999, **397**, 681.
10. B. Messer, J. H. Song, M. Huang, Y. Wu, F. Kim and P. Yang, *Adv. Mater.*, 2000, **12**, 1526-1528.
11. S. Polarz, B. Smarsly and M. Antonietti, *ChemPhysChem*, 2001, **2**, 457-461.
12. F. Camerel, M. Antonietti and C. F. J. Faul, *Chem. Eur. J.*, 2003, **9**, 2160-2166.
13. Y. Jiang, S. Liu, J. Zhang and L. Wu, *Dalton Trans.*, 2013, **42**, 7643-7650.
14. F. Camerel, P. Strauch, M. Antonietti and C. F. J. Faul, *Chem. Eur. J.*, 2003, **9**, 3764-3771.
15. F. Camerel, J. Barbera, J. Otsuki, T. Tokimoto, Y. Shimazaki, L. Y. Chen, S. H. Liu, M. S. Lin, C. C. Wu and R. Ziessel, *Adv. Mater.*, 2008, **20**, 3462-+.
16. F. Camerel, A. Vacher, O. Jeannin, J. Barberá and M. Fourmigué, *Chem. Eur. J.*, 2015, **21**, 19149-19158.
17. S. Ujiie, M. Osaka, Y. Yano and K. Iimura, *Kobunshi Robunshu*, 2000, **57**, 797-802.
18. D. Tsiourvas, T. Felekis, Z. Sideratou and C. M. Paleos, *Liquid Crystals*, 2004, **31**, 739-744.
19. A. G. Cook, U. Baumeister and C. Tschierske, *J. Mater. Chem.*, 2005, **15**, 1708-1721.
20. Y. Chen, Z. Shen, L. Gehringer, H. Frey and S. E. Stürba, *Macromol. Rapid Commun.*, 2005, **27**, 69-75.
21. M. Marcos, R. Alcalá, J. Barberá, P. Romero, C. Sánchez and J. L. Serrano, *Chem. Mater.*, 2008, **20**, 5209-5217.
22. W. Li, W. Bu, H. Li, L. Wu and M. Li, *Chem. Commun.*, 2005, **41**, 3785-3787.
23. Y. Molard, A. Ledneva, M. Amela-Cortes, V. Circu, N. G. Naumov, C. Meriadec, F. Artzner and S. Cordier, *Chem. Mater.*, 2011, **23**, 5122-5130.
24. M. Amela-Cortes, S. Cordier, N. G. Naumov, C. Meriadec, F. Artzner and Y. Molard, *J. Mater. Chem. C*, 2014, **2**, 9813-9823.
25. M. Prevot, M. Amela-Cortes, S. k. Manna, S. Cordier, T. Roisnel, H. Folliot, L. Dupont and Y. Molard, *J. Mater. Chem. C*, 2015, **3**, 5152-5161.
26. M. Prevot, M. Amela-Cortes, S. K. Manna, R. Lefort, S. Cordier, H. Folliot, L. Dupont and Y. Molard, *Adv. Funct. Mater.*, 2015, **25**, 4966-4975.
27. S. M. Wood, M. Prévôt, M. Amela-Cortes, S. Cordier, S. J. Elston, Y. Molard and S. M. Morris, *Adv. Optical Mater.*, 2015, **3**, 1368-1372.
28. Y. Molard, *Acc. Chem. Res.*, 2016, **49**, 1514-1523.
29. A. W. Maverick, J. S. Najdzionek, D. MacKenzie, D. G. Nocera and H. B. Gray, *J. Am. Chem. Soc.*, 1983, **105**, 1878-1882.
30. T. G. Gray, C. M. Rudzinski, D. G. Nocera and R. H. Holm, *Inorg. Chem.*, 1999, **38**, 5932-5933.
31. R. Arratia-Perez and L. Hernandez-Acevedo, *J. Chem. Phys.*, 1999, **110**, 2529-2532.
32. T. G. Gray, C. M. Rudzinski, E. E. Meyer, R. H. Holm and D. G. Nocera, *J. Am. Chem. Soc.*, 2003, **125**, 4755-4770.
33. M. N. Sokolov, M. A. Mihailov, E. V. Peresyphkina, K. A. Brylev, N. Kitamura and V. P. Fedin, *Dalton Trans.*, 2011, **40**, 6375-6377.
34. K. Kirakci, P. Kubat, M. Dusek, K. Fejfarova, V. Sicha, J. Mosinger and K. Lang, *Eur. J. Inorg. Chem.*, 2012, 3107-3111.
35. S. Akagi, S. Fujii and N. Kitamura, *Dalton Trans.*, 2018, **47**, 1131-1139.
36. K. Kirakci, P. Kubát, K. Fejfarová, J. Martinčík, M. Nikl and K. Lang, *Inorg. Chem.*, 2016, **55**, 803-809.
37. A. A. Krasilnikova, A. O. Solovieva, K. E. Trifonova, K. A. Brylev, A. A. Ivanov, S. J. Kim, M. A. Shestopalov, M. S. Fufaeva, A. M. Shestopalov, Y. V. Mironov, A. F. Poveshchenko and L. V. Shestopalova, *Contrast Media Mol. Imaging*, 2016, **11**, 459-466.
38. A. O. Solovieva, K. Kirakci, A. A. Ivanov, P. Kubát, T. N. Pozmogova, S. M. Miroshnichenko, E. V. Vorontsova, A. V. Chechushkov, K. E. Trifonova, M. S. Fufaeva, E. I. Kretov, Y. V. Mironov, A. F. Poveshchenko, K. Lang and M. A. Shestopalov, *Inorganic Chemistry*, 2017, **56**, 13491-13499.
39. A. Garreau, F. Massuyeau, S. Cordier, Y. Molard, E. Gautron, P. Bertocini, E. Faulques, J. Wery, B. Humbert, A. Bulou and J.-L. Duvail, *Acs Nano*, 2013, **7**, 2977-2987.
40. J. Bignon, N. Huby, M. Amela-Cortes, Y. Molard, A. Garreau, S. Cordier, B. Bêche and J. L. Duvail, *Nanotechnology*, 2016, **27**, 255201.
41. N. Huby, J. Bignon, Q. Lagneaux, M. Amela-Cortes, A. Garreau, Y. Molard, J. Fade, A. Desert, E. Faulques, B. Beche, J.-L. Duvail and S. Cordier, *Opt. Mater.*, 2016, **52**, 196-202.
42. P. S. Kuttipillai, Y. Zhao, C. J. Traverse, R. J. Staples, B. G. Levine and R. R. Lunt, *Adv. Mater.*, 2016, **28**, 320-326.
43. J. H. Golden, H. B. Deng, F. J. Disalvo, J. M. J. Frechet and P. M. Thompson, *Science*, 1995, **268**, 1463-1466.
44. L. M. Robinson and D. F. Shriver, *J. Coord. Chem.*, 1996, **37**, 119-129.

45. F. Grasset, F. Dorson, S. Cordier, Y. Molard, C. Perrin, A.-M. Marie, T. Sasaki, H. Haneda, Y. Bando and M. Mortier, *Adv. Mater.*, 2008, **20**, 143-148.
46. Y. Molard, F. Dorson, V. Circu, T. Roisnel, F. Artzner and S. Cordier, *Angew. Chem. Int. Ed. Engl.*, 2010, **49**, 3351-3355.
47. Y. Molard, F. Dorson, K. A. Brylev, M. A. Shestopalov, Y. Le Gal, S. Cordier, Y. V. Mironov, N. Kitamura and C. Perrin, *Chem. Eur. J.*, 2010, **16**, 5613-5619.
48. Y. Molard, C. Labbe, J. Cardin and S. Cordier, *Adv. Funct. Mater.*, 2013, **23**, 4821-4825.
49. M. Amela-Cortes, A. Garreau, S. Cordier, E. Faulques, J.-L. Duvail and Y. Molard, *J. Mater. Chem. C*, 2014, **2**, 1545-1552.
50. M. Robin, W. Kuai, M. Amela-Cortes, S. Cordier, Y. Molard, T. Mohammed-Brahim, E. Jacques and M. Harnois, *ACS Appl. Mater. Interfaces*, 2015, **7**, 21975-21984.
51. S. Cordier, F. Grasset, Y. Molard, M. Amela-Cortes, R. Boukherroub, S. Ravaine, M. Mortier, N. Ohashi, N. Saito and H. Haneda, *J. Inorg. Organomet. Polym. Mater.*, 2015, **25**, 189-204.
52. S. Cordier, Y. Molard, K. A. Brylev, Y. V. Mironov, F. Grasset, B. Fabre and N. G. Naumov, *J. Cluster Sci.*, 2015, **26**, 53-81.
53. A. Beltran, M. Mikhailov, M. N. Sokolov, V. Perez-Laguna, A. Rezusta, M. J. Revillo and F. Galindo, *J. Mater. Chem. B*, 2016, **4**, 5975-5979.
54. M. Robin, N. Dumait, M. Amela-Cortes, C. Roiland, M. Harnois, E. Jacques, H. Folliot and Y. Molard, *Chem. Eur. J.*, 2018, **24**, 4825-4829.
55. J. R. Long, L. S. McCarty and R. H. Holm, *J. Am. Chem. Soc.*, 1996, **118**, 4603-4616.
56. S. Cordier, K. Kirakci, D. Mery, C. Perrin and D. Astruc, *Inorg. Chim. Acta*, 2006, **359**, 1705-1709.
57. M. Amela-Cortes, S. Paofai, S. Cordier, H. Folliot and Y. Molard, *Chem. Commun.*, 2015, **51**, 8177-8180.
58. M. Amela-Cortes, Y. Molard, S. Paofai, A. Desert, J.-L. Duvail, N. G. Naumov and S. Cordier, *Dalton Trans.*, 2016, **45**, 237-245.
59. T. Wöhrle, I. Wurzbach, J. Kirres, A. Kostidou, N. Kapernaum, J. Litterscheidt, J. C. Haenle, P. Staffeld, A. Baro, F. Giesselmann and S. Laschat, *Chem. Rev.*, 2016, **116**, 1139-1241.
60. S. Kumar, *Chemistry of Discotic Liquid Crystals: From Monomers to Polymers*, CRC Press, Boca Raton, USA, 2011.
61. J. W. Goodby, P. J. Collings, T. Kato, C. Tschierske, H. F. Gleeson, P. Raynes and Editors, *Handbook of Liquid Crystals, Volume 8: Applications of Liquid Crystals, 2nd Edition*, Wiley-VCH Verlag GmbH & Co. KGaA, 2014.
62. S. K. Nayak, M. Amela-Cortes, M. M. Neidhardt, S. Beardsworth, J. Kirres, M. Mansueto, S. Cordier, S. Laschat and Y. Molard, *Chem. Commun.*, 2016, **52**, 3127 - 3130.
63. S. Kumar, *Liquid Crystals*, 2004, **31**, 1037-1059.
64. R. K. Gupta, V. Manjuladevi, C. Karthik and K. Choudhary, *Liquid Crystals*, 2016, **43**, 2079-2091.
65. A. N. Cammidge, H. Gopee and H. Patel, *Tetrahedron Lett.*, 2009, **50**, 3513-3515.
66. S. Kumar and M. Manickam, *Synthesis*, 1998, **1998**, 1119-1122.
67. J. Malthête, H. T. Nguyen and C. Destrade, *Liquid Crystals*, 1993, **13**, 171-187.
68. H.-T. Nguyen, C. Destrade and J. Malthete, *Adv. Mater.*, 1997, **9**, 375-388.
69. D. Fazio, C. Mongin, B. Donnio, Y. Galerne, D. Guillon and D. W. Bruce, *J. Mater. Chem.*, 2001, **11**, 2852-2863.
70. C. Destrade, M. C. Mondon and J. Malthete, *J. Phys. Colloques*, 1979, **40**, C3-17-C13-21.
71. F. Camerel, F. Barrière and O. Jeannin, *Liquid Crystals*, 2018, **45**, 698-702.
72. D. Guillon, *Struct. Bonding*, 1999, **95**, 41-82.
73. S. Kumar and S. K. Pal, *Tetrahedron Letters*, 2005, **46**, 2607-2610.
74. S. Kumar and S. K. Gupta, *Tetrahedron Lett.*, 2010, **51**, 5459-5462.
75. A. B. Miguel-Coello, M. Bardaji, S. Coco, B. Donnio, B. Heinrich and P. Espinet, *Inorg. Chem.*, 2018, **57**, 4359-4369.
76. M. A. Alam, J. Motoyanagi, Y. Yamamoto, T. Fukushima, J. Kim, K. Kato, M. Takata, A. Saeki, S. Seki, S. Tagawa and T. Aida, *J. Am. Chem. Soc.*, 2009, **131**, 17722-17723.
77. J. Motoyanagi, T. Fukushima and T. Aida, *Chem. Commun.*, 2005, 101-103.
78. M. Funahashi, H. Shimura, M. Yoshio and T. Kato, *Struct. Bonding*, 2007, **128**, 151-179.
79. F. Camerel, B. Donnio, C. Bourgogne, M. Schmutz, D. Guillon, P. Davidson and R. Ziessel, *Chem. Eur. J.*, 2006, **12**, 4261-4274.
80. R. Ziessel, L. Douce, A. El-Ghayoury, A. Harriman and A. Skoulios, *Angew. Chem., Int. Ed.*, 2000, **39**, 1489-1493.
81. K.-Q. Zhao, L.-L. An, X.-B. Zhang, W.-H. Yu, P. Hu, B.-Q. Wang, J. Xu, Q.-D. Zeng, H. Monobe, Y. Shimizu, B. Heinrich and B. Donnio, *Chem. Eur. J.*, 2015, **21**, 10379-10390.
82. I. Tahar-Djebbar, F. Nekelson, B. Heinrich, B. Donnio, D. Guillon, D. Kreher, F. Mathevet and A.-J. Attias, *Chem. Mater.*, 2011, **23**, 4653-4656.
83. C. P. Umesh, A. T. M. Marcelis and H. Zuilhof, *Liq. Cryst.*, 2015, **42**, 1450-1459.
84. K.-Q. Zhao, X.-Y. Bai, B. Xiao, Y. Gao, P. Hu, B.-Q. Wang, Q.-D. Zeng, C. Wang, B. Heinrich and B. Donnio, *J. Mater. Chem. C*, 2015, **3**, 11735-11746.
85. C. Guilbaud, A. Deluzet, B. Domercq, P. Molinie, C. Coulon, K. Boubekeur and P. Batail, *Chem. Commun.*, 1999, 1867-1868.
86. K. Kirakci, K. Fejfarova, M. Kucerakova and K. Lang, *Eur. J. Inorg. Chem.*, 2014, **14**, 2331-2336.
87. D. Markovitsi, I. Lecuyer, P. Lianos and J. Malthete, *J. Chem. Soc., Faraday Trans.*, 1991, **87**, 1785-1790.
88. D. Markovitsi, A. Germain, P. Millie, P. Lecuyer, L. Gallos, P. Argyrakakis, H. Bengs and H. Ringsdorf, *The Journal of Physical Chemistry*, 1995, **99**, 1005-1017.

89. E. Bordes, A. J. L. Costa, J. Szala-Bilnik, J.-M. Andanson, J. M. S. S. Esperanca, M. F. C. Gomes, J. N. C. Lopes and A. A. H. Padua, *Phys. Chem. Chem. Phys.*, 2017, **19**, 27694-27703.
90. H. Bouas-Laurent, A. Castellán, J.-P. Desvergne and R. Lapouyade, *Chem. Soc. Rev.*, 2000, **29**, 43-55.
91. H. Bouas-Laurent, A. Castellán, J.-P. Desvergne and R. Lapouyade, *Chem. Soc. Rev.*, 2001, **30**, 248-263.
92. Y. Molard, D. M. Bassani, J.-P. Desvergne, N. Moran and J. H. R. Tucker, *J. Org. Chem.*, 2006, **71**, 8523-8531.
93. D. Markovitsi, F. Rigaut, M. Mouallem and J. Malthête, *Chem. Phys. Lett.*, 1987, **135**, 236-242.
94. D. Markovitsi, A. Germain, P. Millie, P. Lecuyer, L. Gallos, P. Argyrakis, H. Bengs and H. Ringsdorf, *J. Phys. Chem.*, 1995, **99**, 1005-1017.
95. M. Ikeda, M. Takeuchi and S. Shinkai, *Chem. Commun.*, 2003, 1354-1355.
96. T. Yoshimura, S. Ishizaka, Y. Sasaki, H. B. Kim, N. Kitamura, N. G. Naumov, M. N. Sokolov and V. E. Fedorov, *Chem. Lett.*, 1999, 1121-1122.

## TOC



The ionic association of hexanuclear anionic  $[\text{Re}_6\text{Se}_8(\text{CN})_6]^{4-}$  clusters with imidazolium ion-anchored triphenylene generates original air stable red phosphorescent columnar mesophases with good film-forming properties

# Ionic Columnar Clustomesogens: Associations between Anionic Hexanuclear Rhenium Clusters and Liquid Crystalline Triphenylene Tethered Imidazoliums

## Supplementary information.

Characterizations.....	3
Synthesis.....	4
Supplementary figures .....	7
<b>Figure S1.</b> DSC traces of <b>TP1Br</b> (Top: 2 <sup>nd</sup> and 3 <sup>rd</sup> heating curves, bottom: 1 <sup>st</sup> and 2 <sup>nd</sup> cooling curves, scan rate: 10°C/min).....	7
<b>Figure S2.</b> <b>TP1Br</b> compound observed by optical microscopy between crossed-polarizers at 95 °C upon cooling from the isotropic state (crossed-polarizers symbolized by the white cross in the corner of the picture).....	8
<b>Figure S3.</b> SAXS pattern of <b>TP1Br</b> compound recorded at 100 °C (2 <sup>nd</sup> heating curve). .....	8
<b>Figure S4.</b> Temperature-dependent SAXS patterns of <b>TP1Br</b> . .....	8
<b>Figure S5.</b> SAXS pattern of 2,3,6,7,10,11-hexakis(pentyloxy)triphenylene compound at 90 °C.....	9
<b>Figure S6.</b> DSC traces of <b>TP2Br</b> (Top: 2 <sup>nd</sup> and 3 <sup>rd</sup> heating curves, bottom: 1 <sup>st</sup> and 2 <sup>nd</sup> cooling curves, scan rate: 10°C/min).....	9
<b>Figure S7.</b> Optical photomicrograph of <b>TP2Br</b> obtained with a polarizing microscope on cooling from the isotropic liquid at 80 °C (crossed-polarizers symbolized by the white cross in the corner of the picture).....	10
<b>Figure S8.</b> SAXS pattern of <b>TP2Br</b> compound recorded at 70 °C (2 <sup>nd</sup> heating curve). .....	10
<b>Figure S9.</b> DSC traces of <b>Cplx1</b> compound (Top: 2 <sup>nd</sup> and 3 <sup>rd</sup> heating curves, bottom: 1 <sup>st</sup> and 2 <sup>nd</sup> cooling curves, scan rate: 10°C/min).....	11
<b>Figure S10.</b> POM images of <b>Cplx1</b> compound obtained at 191 °C upon cooling from the isotropic state (crossed-polarizers symbolized by the white cross in the corner of the picture).....	11
<b>Figure S11.</b> SAXS pattern of <b>Cplx1</b> recorded at 140 °C (2 <sup>nd</sup> heating curve). .....	12
<b>Figure S12.</b> DSC traces of <b>Cplx2</b> compound (Top: 2 <sup>nd</sup> and 3 <sup>rd</sup> heating curves, bottom: 1 <sup>st</sup> and 2 <sup>nd</sup> cooling curves, scan rate: 10°C/min).....	12
<b>Figure S13.</b> Optical photomicrograph of <b>Cplx2</b> obtained with a polarizing microscope at: a) 120 °C in the isotropic phase, b) 84 °C upon slow cooling from the isotropic phase and c) 84 °C after gentle pressure on the glass slide (crossed-polarizers symbolized by the white cross in the corner of the picture). .....	13
<b>Figure S14.</b> SAXS patterns of <b>Cplx2</b> recorded at 80 °C.....	14
<b>Figure S15.</b> Absorption spectra of <b>TP1Br</b> , <b>TP2Br</b> , <b>Cplx1</b> and <b>Cplx2</b> in dichloromethane ( $c \sim 10^{-6}$ M) .....	14
<b>Figure S16.</b> Normalized emission spectra in aerated dichloromethane of <b>TP1Br</b> , <b>TP2Br</b> , <b>Cplx1</b> and <b>Cplx2</b> upon excitation at 310 nm. ....	14

<b>Figure S17.</b> Emission spectra in deaerated dichloromethane of <b>TP1Br</b> , upon excitation at a) 320 nm, b) 350 nm, c) 360 nm, d) 365 nm, e) 370 nm, f) 375 nm and g) 380 nm. ....	15
<b>Figure S18.</b> Emission spectra in deaerated dichloromethane of <b>TP2Br</b> , upon excitation at a) 320 nm, b) 350 nm, c) 360 nm, d) 365 nm, e) 370 nm, f) 375 nm and g) 380 nm. ....	15
<b>Figure S19.</b> Integrated luminescence decay profile of <b>TP1Br</b> in dichloromethane; inset: corresponding emission decay map.....	16
<b>Figure S20.</b> Integrated luminescence decay profile of <b>TP2Br</b> in dichloromethane; inset: corresponding emission decay map.....	16
<b>Figure S21.</b> Integrated luminescence decay profiles of <b>Cplx1</b> in deaerated dichloromethane; inset: corresponding emission decay map between 382 and 518 nm. ....	17
<b>Figure S22.</b> Integrated luminescence decay profiles of <b>Cplx1</b> in deaerated dichloromethane; inset: corresponding emission decay map between 642 and 778 nm. ....	17
<b>Figure S23.</b> Integrated luminescence decay profiles of <b>Cplx2</b> in deaerated dichloromethane; inset: corresponding emission decay map between 382 and 518 nm. ....	18
<b>Figure S24.</b> Integrated luminescence decay profiles of <b>Cplx2</b> in deaerated dichloromethane; inset: corresponding emission decay map between 642 and 778 nm. ....	18
<b>Figure S25.</b> Solid state integrated luminescence decay profile of <b>TP1Br</b> ; inset: corresponding emission decay map. ....	19
<b>Figure S26.</b> Solid state integrated luminescence decay profile of <b>TP2Br</b> ; inset: corresponding emission decay map. ....	19
<b>Figure S27.</b> Solid state integrated luminescence decay profile of <b>Cplx1</b> ; inset: corresponding emission decay map. ....	20
<b>Figure S28.</b> Solid state integrated luminescence decay profile of <b>Cplx2</b> ; inset: corresponding emission decay map. ....	20

## Characterizations.

**300 (<sup>1</sup>H) and 75.5 MHz (<sup>13</sup>C) NMR spectra** were recorded on Bruker Avance 300 spectrometer at room temperature using perdeuterated solvents as internal standards. Elemental analyses were performed by the service central d'analyses du CNRS, Vernaison, France. Mass spectra were recorded with a MALDI-TOF Microflex LT Bruker. UV-Vis spectra were recorded using a UV-3600 plus UV-Vis-NIR spectrophotometer (Shimadzu). Absolute quantum yield were measured with a Hamamatsu C9920-03G system.

**Differential scanning calorimetry (DSC)** was carried out by using NETZSCH DSC 200 F3 instrument equipped with an intracooler. DSC traces were measured at 10 °C/min down to -25 °C.

**Optical microscopy** investigations were performed on a Nikon H600L polarizing microscope equipped with a Linkam "liquid crystal pro system" hotstage LTS420. The microscope is also equipped with a UV irradiation source (Hg Lamp,  $\lambda = 340\text{-}380$  nm) and an ocean optic USB 2000+ UV-Vis-NIR spectrophotometer based on CCD detection technology.

**X-ray scattering experiments (SAXS)** were performed using a FR591 Bruker AXS rotating anode X-ray generator operated at 40 kV and 40 mA with monochromatic Cu K $\alpha$  radiation ( $\lambda = 1.541$  Å) and point collimation. The patterns were collected with a Mar345 Image-Plate detector (Marresearch, Norderstedt, Germany). The samples were held in Lindeman glass capillaries (1 mm diameter). The capillaries were placed inside a Linkam HFX350-Capillary X-Ray stage which allow measurements from -196 °C up to 350 °C with an accuracy of 0.1 °C.

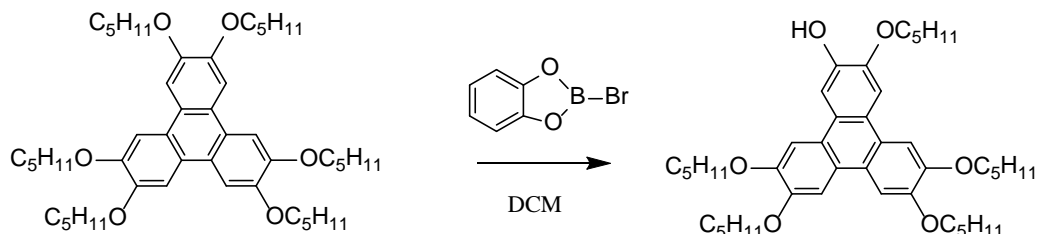
**Emission measurements.** Lifetime measurements and TRPL mapping were realized using a picosecond laser diode (Jobin Yvon deltadiode, 375 nm) and a Hamamatsu C10910-25 streak camera mounted with a slow single sweep unit. Signals were integrated on a 30 nm bandwidth. Fits were obtained using origin software and the goodness of fit judge by the reduced  $\chi^2$  value and residual plot shape. The luminescence spectra in deaerated dichloromethane and absolute quantum yields in the solid state were measured with a C9920-03 Hamamatsu system equipped with a 150 W xenonlamp, a monochromator, an integrating sphere and a red-NIR sensitive PMA-12 detector.

**SCLC Measurements.** Devices were prepared by evaporating 50 nm thick gold on SU8 (epoxy photosensitive commercial ink, SU8 2000.5) pre-coated glasses. Then gold was patterned by photolithography process to shape the electrodes. The distances between two electrodes, equal to 3  $\mu\text{m}$ , define the semiconductor (SC) thickness of the coplanar Au-SC-Au diode. Finally, the compounds were aligned on the electrode under polarised microscope. All electrical characterizations were performed in the dark under nitrogen atmosphere using a 2636A Keithley.

## Synthesis.

$K_4Re_6Se_8(CN)_6 \cdot 3.5H_2O$  <sup>[1]</sup> and 2,3,6,7,10,11-hexakis(pentyloxy)triphenylene<sup>[2]</sup> were synthesized as already reported.

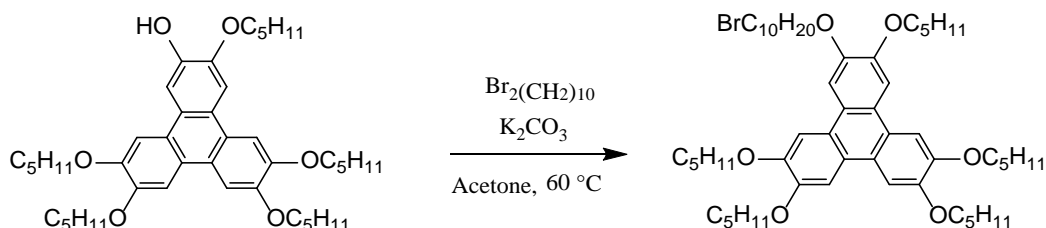
### Compound 1



2,3,6,7,10,11-hexakis(pentyloxy)triphenylene (0.452 g, 0.6 mmol) was dissolved in 20 mL anhydrous dichloromethane. 1.82 mL of a 0.5M *B*-Bromocatecholborane in  $CH_2Cl_2$  (1.5 eq) was added to the mixture. The solution was stirred under nitrogen at room temperature for 48 hours. After that, the solution was washed two times with water (50 mL) and one time with brine (50 mL) and dried over  $MgSO_4$  before removal of the solvent. The compound was purified by flash chromatography on silica gel with petroleum ether/Ethyl acetate (100/0 to 95/5) as eluent. The product was isolated after removal of the solvent as a black oil (0.196 g, 48 % yield).

$^1H$  NMR (300 MHz, Chloroform-*d*)  $\delta$  7.53-8.06 (m, CH, 6H), 5.90 (s, 1H, OH), 4.09-4.36 (m,  $OCH_2$ , 10H), 1.85-2.05 (m,  $CH_2$ , 10H), 1.34-1.67 (m,  $CH_2$ , 20H), 0.80-1.11 (m,  $CH_3$ , 15H).

### Compound 2



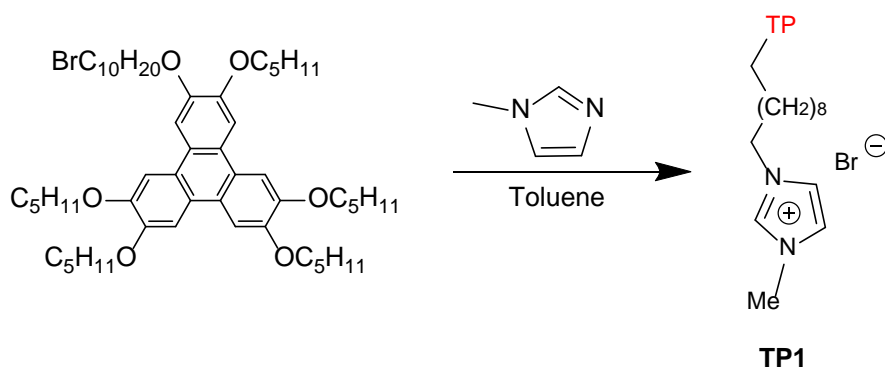
To a solution of compound **1** (0.652 g, 0.97 mmol) and  $K_2CO_3$  (0.877 g, 10 eq) in 30 mL acetone, 5 equivalents of 1,10-dibromodecane (1.44 g, 4.85 mmol) were added. The reaction mixture was heated at 60 °C under  $N_2$  for 12 hours. After that, 30 mL of water was added and the solution was extracted with  $CH_2Cl_2$  (3x30mL). The organic phase was dried over  $MgSO_4$  and after removal of the solvent, the product was purified by flash chromatography on silica gel using a solvent gradient from pure petroleum ether to pure dichloromethane. The product was isolated as a black oil in 78 % yield (0.665 g).

$^1H$  NMR (300 MHz, Chloroform-*d*)  $\delta$  7.85 (s, 6H, CH), 4.25 (t,  $J = 6.6$  Hz, 12H,  $OCH_2$ ), 3.39 (t,  $J = 6.9$  Hz, 2H,  $CH_2Br$ ), 1.98 (p,  $J = 6.8$  Hz, 12H,  $CH_2$ ), 1.72 – 1.24 (m, 34H,  $CH_2$ ), 1.00 (t,  $J = 7.2$  Hz, 15H,  $CH_3$ );  $^{13}C$  NMR (75 MHz,  $CDCl_3$ )  $\delta$  148.97 (Cq), 123.63 (Cq), 107.27 (CH), 69.68, 34.06, 32.90, 29.62, 29.55, 29.48, 29.23, 28.87, 28.46, 28.24, 26.26, 22.67, 14.21 ( $CH_3$ ).

<sup>1</sup> N. G. Naumov, A. V. Virovets, N. V. Podberezskaya, V. E. Fedorov, *J. Struct. Chem.*, 1997, **38**, 857–862.

<sup>2</sup> A.N. Cammidge, H. Gopee, H. Patel, *Tetrahedron Lett.* 2009, **50**, 3513–3515

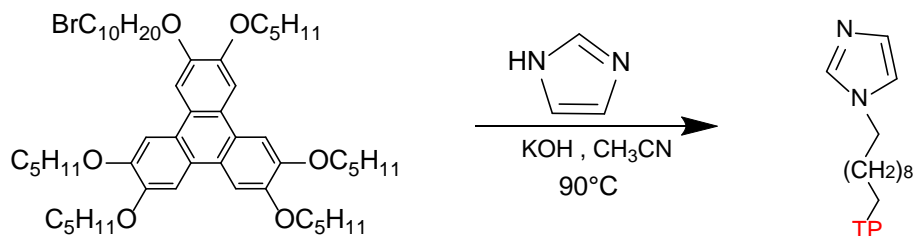
### Compound TP1Br



Compound **2** (0.303 g) was dissolved in 15 mL of toluene (HPLC grade) together with 3 mL of 1-methylimidazole (large excess). The reaction mixture was heated at 120 °C under N<sub>2</sub> for 4 days. After cooling, the solvent was removed and the product was purified by flash column chromatography on alumina gel with DCM/MeOH mixtures (100:0 to 100:10). The product was crystallized by slow evaporation of DCM from a DCM/acetonitrile mixture. Compound **TP1** was isolated as gray salt in 73 % yield after drying.

<sup>1</sup>H NMR (300 MHz, Chloroform-d) δ 10.26 (s, 1H, CH), 7.80 (s, 6H, CH), 7.34 (d, J = 1.7 Hz, 1H, CH), 7.19 (d, J = 1.5 Hz, 1H, CH), 4.21 (q, J = 6.6, 5.6 Hz, 14H, OCH<sub>2</sub> + NCH<sub>2</sub>), 4.02 (s, 3H, NCH<sub>3</sub>), 1.99 – 1.74 (m, 12H, OCH<sub>2</sub>), 1.66 – 1.17 (m, 34H), 1.06 – 0.78 (m, 15H, CH<sub>3</sub>). <sup>13</sup>C NMR (75 MHz, Chloroform-d) δ 149.10 (Cq), 149.08 (Cq), 149.05 (Cq), 137.96 (CH), 123.67 (Cq), 123.64 (Cq), 123.38 (CH), 121.58 (CH), 107.52 (CH), 107.41 (CH), 69.84 (OCH<sub>2</sub>), 69.78 (OCH<sub>2</sub>), 50.15 (NCH<sub>2</sub>), 36.71 (NCH<sub>3</sub>), 30.32 (CH<sub>2</sub>), 29.52 (CH<sub>2</sub>), 29.48 (CH<sub>2</sub>), 29.42 (CH<sub>2</sub>), 29.35 (CH<sub>2</sub>), 29.20 (CH<sub>2</sub>), 29.03 (CH<sub>2</sub>), 28.43 (CH<sub>2</sub>), 26.31 (CH<sub>2</sub>), 26.16 (CH<sub>2</sub>), 25.89 (CH<sub>2</sub>), 22.61 (CH<sub>2</sub>), 14.15 (CH<sub>3</sub>). Anal. Calcd for C<sub>57</sub>H<sub>87</sub>BrN<sub>2</sub>O<sub>6</sub>, H<sub>2</sub>O: C, 68.86; H, 9.02; N, 2.82; Found C, 68.26; H, 9.12; N, 2.71. MALDI-TOF (m/z): 895.3 (100 %) [M]<sup>+</sup>.

### Compound TP'

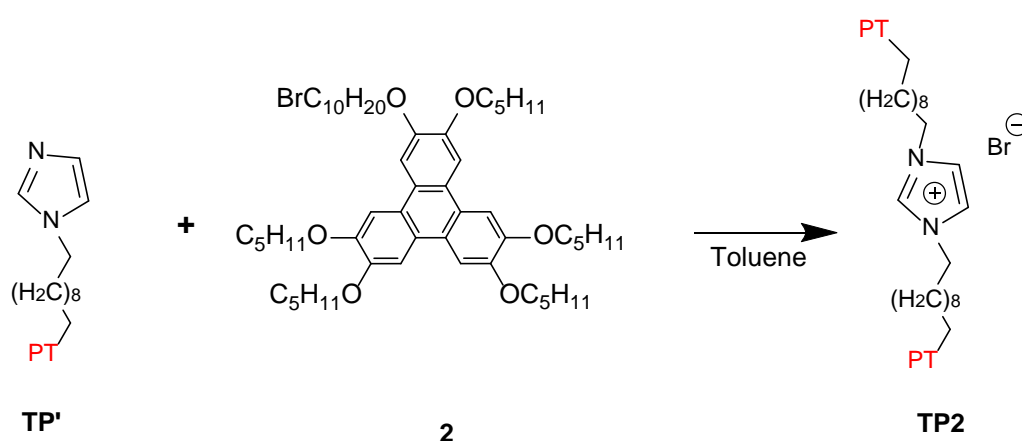


Compound **2** (0.277 g, 0.3 mmol) was dissolved in acetonitrile (10 mL) together with KOH (0.035g, 2 eq) and imidazole (0.021 g, 1 eq). The reaction mixture was heated at 90°C under nitrogen for 48 hours. After cooling, acetonitrile was evaporated and the residue was dissolved in DCM (20 mL). The

solution was washed with water (3x20 mL) and dried over MgSO<sub>4</sub>. The compound was purified by flash chromatography on silica gel with DCM/MeOH mixtures (100:0 to 98:2). After removal of the solvent, the product was isolated as a white powder in 67 % yield (0.185 g).

<sup>1</sup>H NMR (300 MHz, Chloroform-*d*) δ 7.84 (s, CH, 6H), 7.46 (s, CH, 1H), 7.05 (s, CH, 1H), 6.88 (s, CH, 1H), 4.23 (t, OCH<sub>2</sub>, J<sub>HH</sub>= 6.6 Hz, 12H), 3.88 (t, NCH<sub>2</sub>, 2H, J<sub>HH</sub>= 7.2 Hz), 1.94 (m, CH<sub>2</sub>, 12H), 1.19–1.69 (m, CH<sub>2</sub>, 36H), 0.98 (m, CH<sub>3</sub>, 15H).

### Compound TP2Br



**TP'** (0.185 g, 0.2 mmol) and compound **2** (0.188 g, 1 eq) were dissolved in 20 mL toluene (HPLC grade). The reaction mixture was heated at 120 °C under nitrogen for 6 days. After cooling, the toluene was removed and the compound was purified by flash chromatography on alumina gel with DCM/MeOH mixtures (100:0 to 1:99). The product was crystallized by slow evaporation of DCM from a DCM/acetonitrile mixture. Compound **TP2** was isolated as dark-gray salt in 85 % yield after drying.

<sup>1</sup>H NMR (300 MHz, Chloroform-*d*) δ 10.66 (s, 1H, CH), 7.81 (d, J = 2.9 Hz, 12H, CH), 7.11 (d, J = 1.5 Hz, 2H, CH), 4.21 (t, J = 6.6 Hz, 28H, OCH<sub>2</sub> + NCH<sub>2</sub>), 1.93 (p, J = 6.8 Hz, 24H, CH<sub>2</sub>), 1.72 – 1.11 (m, 68H, CH<sub>2</sub>), 0.96 (t, J = 7.1 Hz, 30H, CH<sub>3</sub>). <sup>13</sup>C NMR (75 MHz, Chloroform-*d*) δ 149.18 (Cq), 149.14 (Cq), 123.77 (CH), 121.19 (CH), 107.53 (CH), 69.87 (OCH<sub>2</sub>), 50.36 (NCH<sub>2</sub>), 30.43 (CH<sub>2</sub>), 29.52 (CH<sub>2</sub>), 29.40 (CH<sub>2</sub>), 29.29 (CH<sub>2</sub>), 29.09 (CH<sub>2</sub>), 28.52 (CH<sub>2</sub>), 26.40 (CH<sub>2</sub>), 26.22 (CH<sub>2</sub>), 22.71 (CH<sub>2</sub>), 14.24 (CH<sub>3</sub>). Anal. Calcd for C<sub>109</sub>H<sub>165</sub>BrN<sub>2</sub>O<sub>12</sub>, 0.5CH<sub>2</sub>Cl<sub>2</sub>: C, 72.35; H, 9.20; N, 1.54; Found C, 72.07; H, 9.47; N, 1.74. MALDI-TOF (m/z): 1695.7 (100 %) [M]<sup>+</sup>.

### **General procedure for the synthesis of [Re<sub>6</sub>Se<sub>8</sub>(CN)<sub>6</sub>]<sup>4+</sup> ion associates with TP1 and TP2:**

The cluster salt K<sub>4</sub>[Re<sub>6</sub>Se<sub>8</sub>(CN)<sub>6</sub>·4H<sub>2</sub>O] (1 equiv, 0.025 mmol) was dissolved in DMF (3 mL) and the imidazolium ion-anchored triphenylene (**TP1** or **TP2**) (4 equiv) was added. The mixture was stirred at 60 °C for one night under nitrogen atmosphere. After cooling, water (30 mL)

was then added and the precipitate was filtered, washed with water and dried under vacuum. The product was finally dissolved in  $\text{CH}_2\text{Cl}_2$  and filtered over celite and isolated after removal of the solvent as thin solid films.

**Cplx1:**  $(\text{TP1})_4[\text{Re}_6\text{Se}_8(\text{CN})_6]$ : 85%, Anal. Calcd for  $\text{C}_{234}\text{H}_{348}\text{N}_{14}\text{O}_{24}\text{Re}_6\text{Se}_8$ ,  $\text{CH}_2\text{Cl}_2$ : C, 50.63; H, 6.33; N, 3.52; Found C, 50.31; H, 6.53; N, 3.57. EDX (atomic%): C, 87.05; O, 9.77; Se, 1.87; Re, 1.31.

**Cplx2:**  $(\text{TP2})_4[\text{Re}_6\text{Se}_8(\text{CN})_6]$ : 53%, Anal. Calcd for  $\text{C}_{442}\text{H}_{660}\text{N}_{14}\text{O}_{48}\text{Re}_6\text{Se}_8$ ,  $\text{CH}_2\text{Cl}_2$ : C, 60.66; H, 7.61; N, 2.24; Found C, 60.27; H, 7.77; N, 2.41. EDX (atomic%): C, 85.65; O, 12.65; Se, 1.00; Re, 0.71.

### Supplementary figures

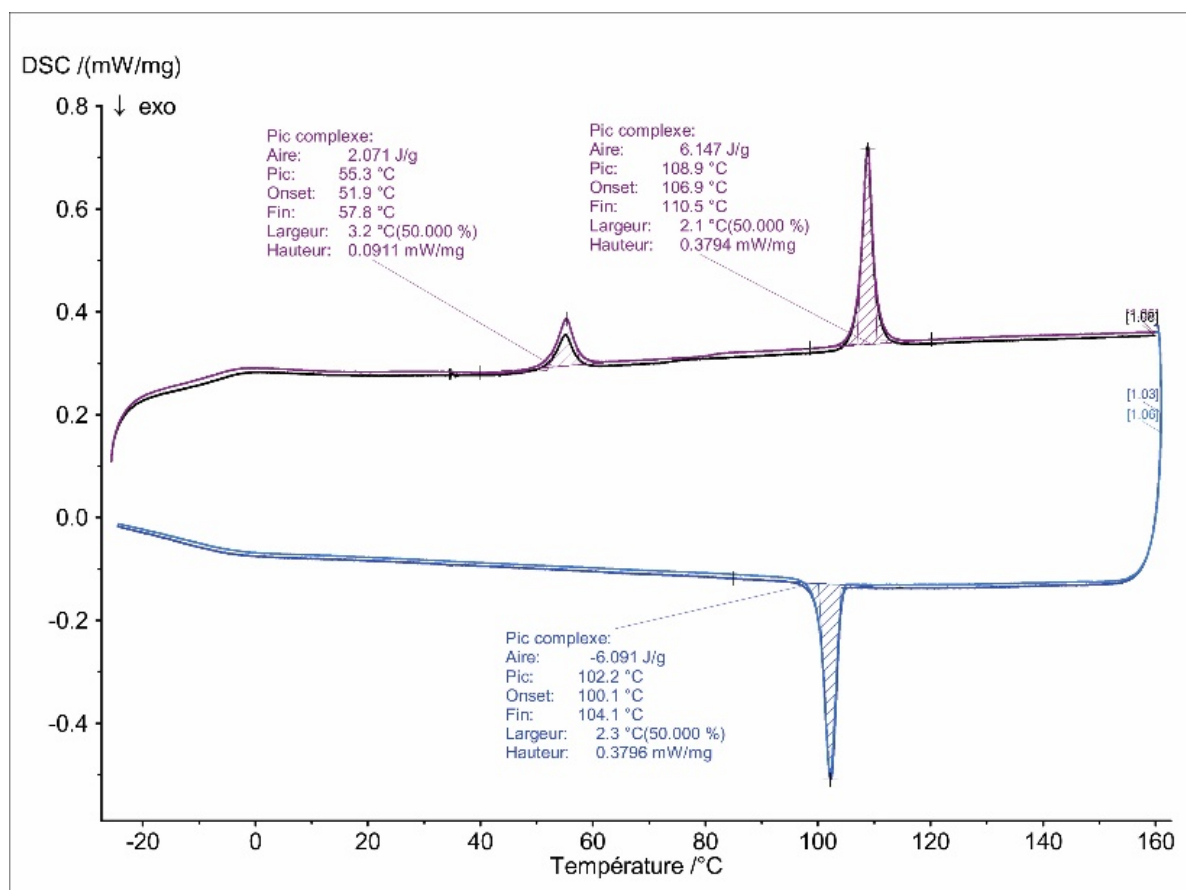


**Figure S1.** DSC traces of TP1Br (Top: 2<sup>nd</sup> and 3<sup>rd</sup> heating curves, bottom: 1<sup>st</sup> and 2<sup>nd</sup> cooling curves, scan rate: 10°C/min).

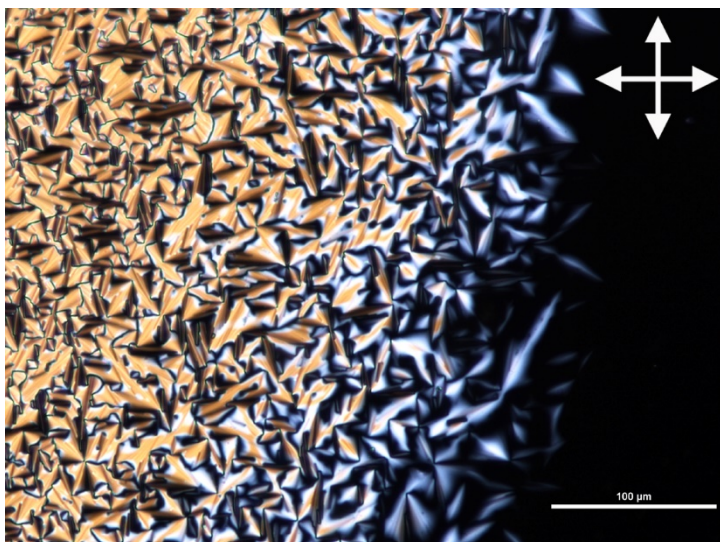


**Figure S2.** TP1Br compound observed by optical microscopy between crossed-polarizers at 95 °C upon cooling from the isotropic state (crossed-polarizers symbolized by the white cross in the corner of the picture).

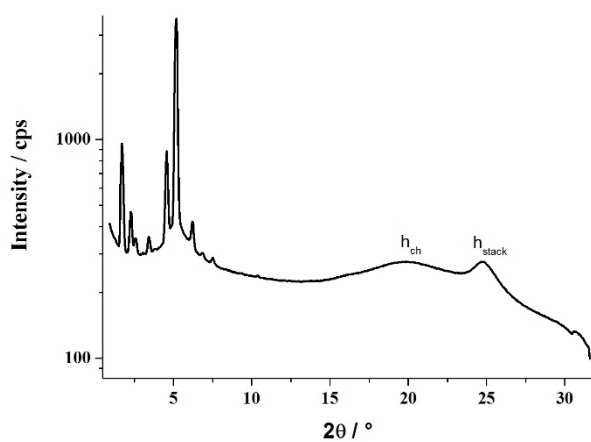


**Figure S3.** SAXS pattern of TP1Br compound recorded at 100 °C (2<sup>nd</sup> heating curve).

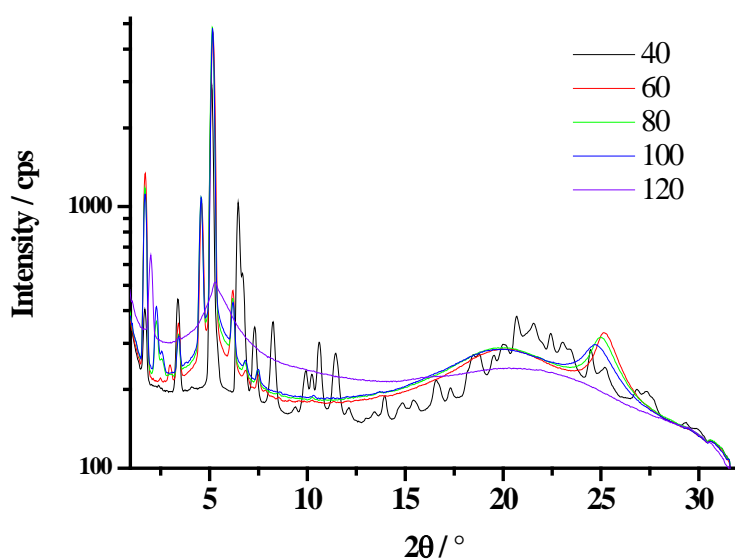


**Figure S4.** Temperature-dependent SAXS patterns of TP1Br.

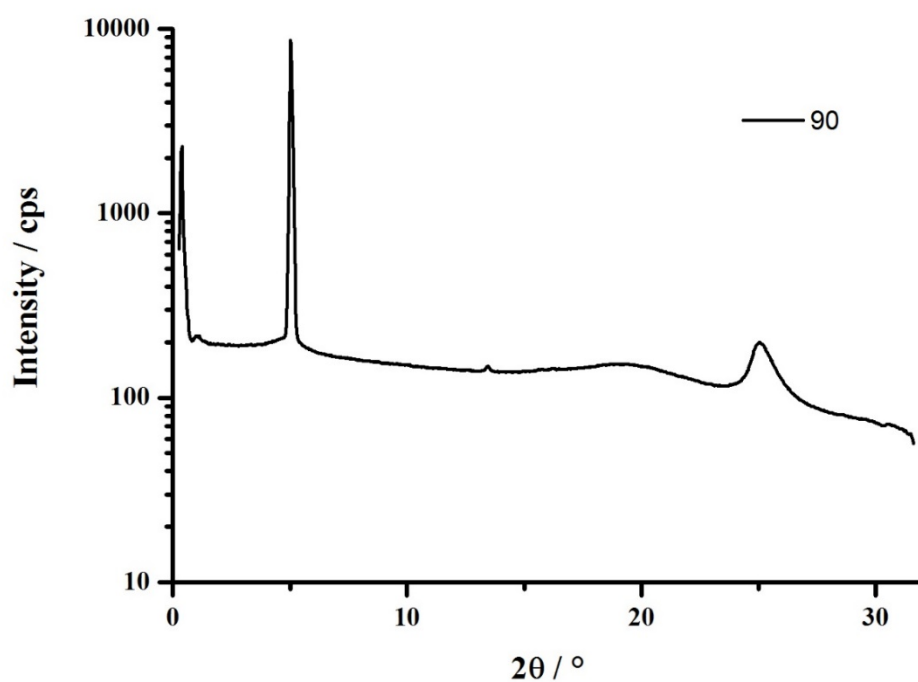


**Figure S5.** SAXS pattern of 2,3,6,7,10,11-hexakis(pentyloxy)triphenylene compound at 90 °C.

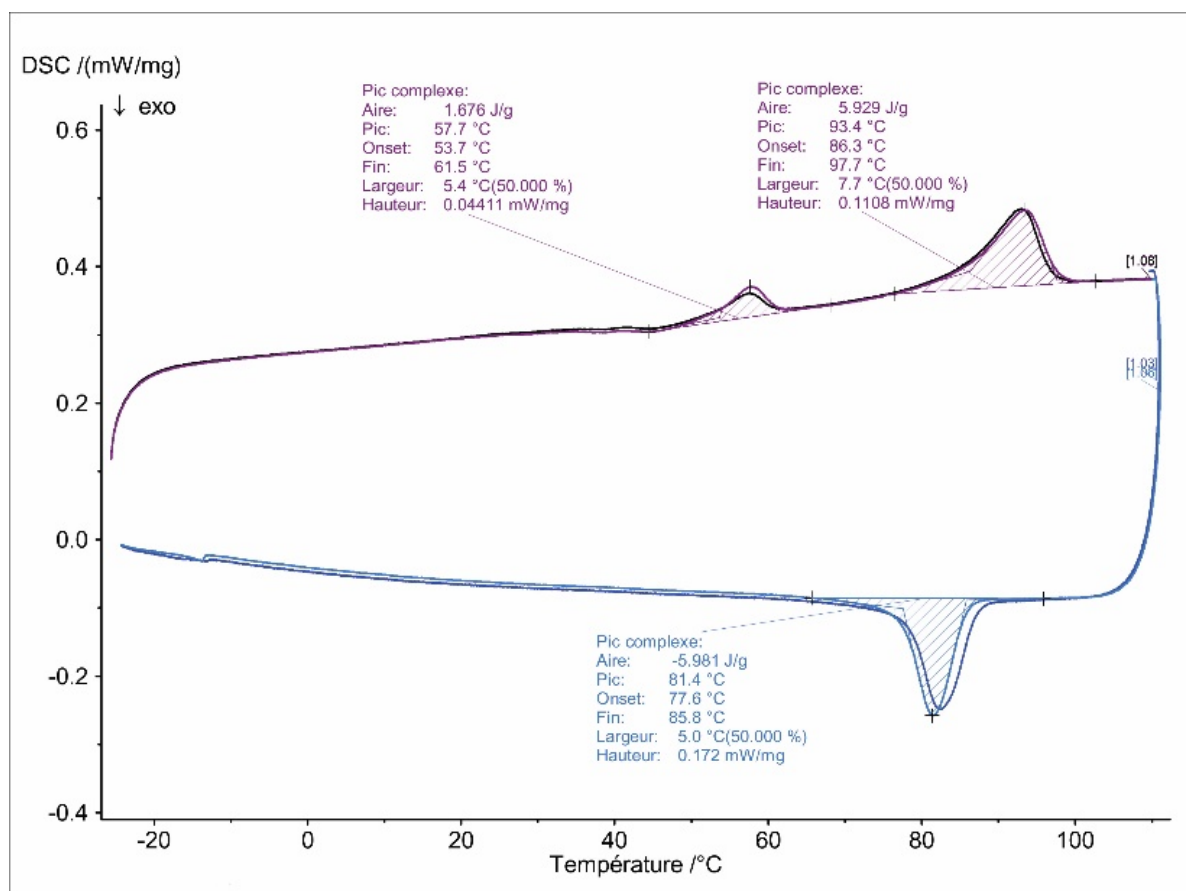


**Figure S6.** DSC traces of TP2Br (Top: 2<sup>nd</sup> and 3<sup>rd</sup> heating curves, bottom: 1<sup>st</sup> and 2<sup>nd</sup> cooling curves, scan rate: 10°C/min).

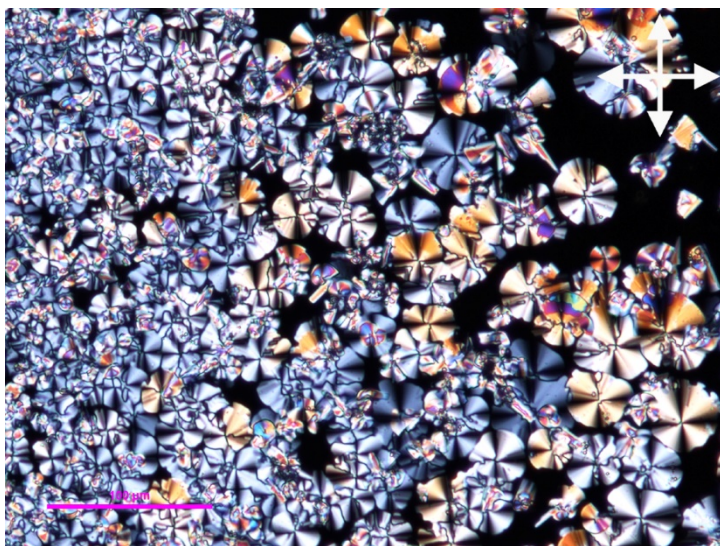


**Figure S7.** Optical photomicrograph of **TP2Br** obtained with a polarizing microscope on cooling from the isotropic liquid at 80 °C (crossed-polarizers symbolized by the white cross in the corner of the picture).

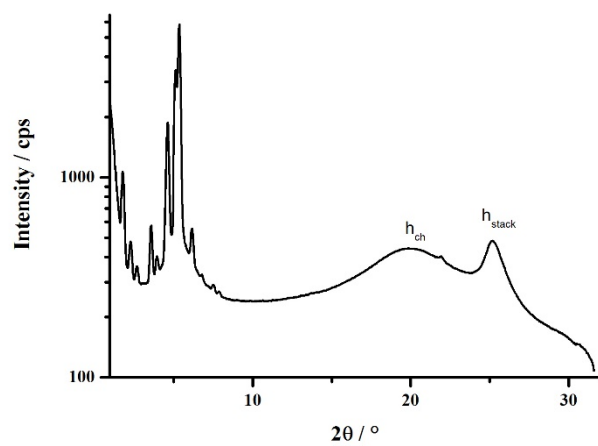


**Figure S8.** SAXS pattern of **TP2Br** compound recorded at 70 °C (2<sup>nd</sup> heating curve).

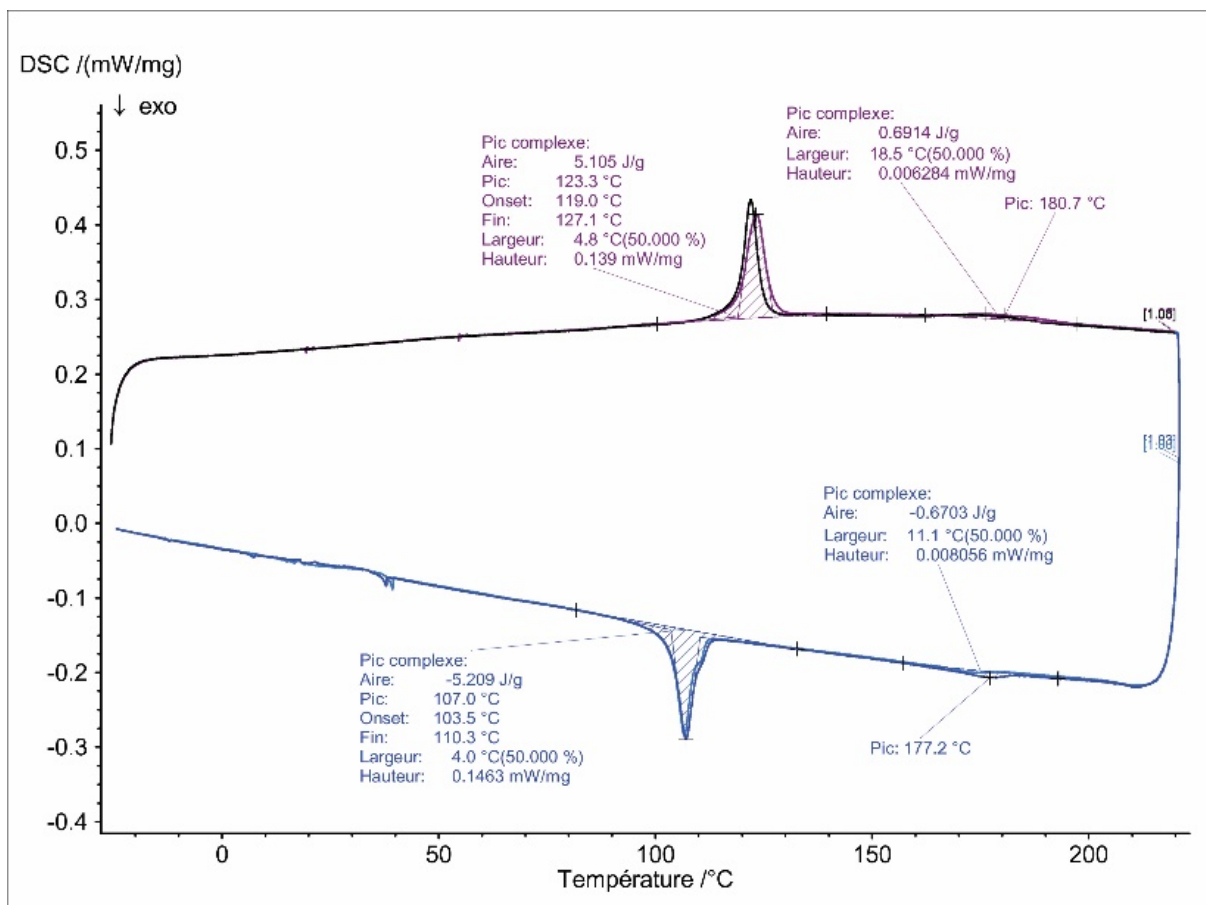


**Figure S9.** DSC traces of **Cplx1** compound (Top: 2<sup>nd</sup> and 3<sup>rd</sup> heating curves, bottom: 1<sup>st</sup> and 2<sup>nd</sup> cooling curves, scan rate: 10°C/min).

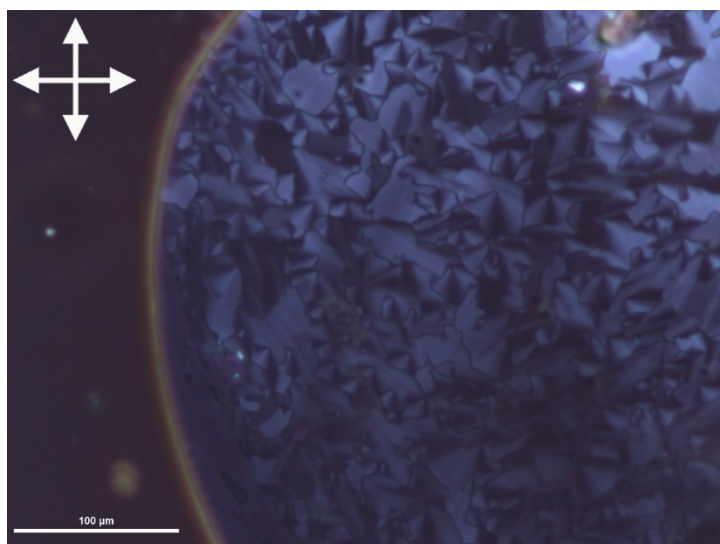


**Figure S10.** POM images of **Cplx1** compound obtained at 191 °C upon cooling from the isotropic state (crossed-polarizers symbolized by the white cross in the corner of the picture).

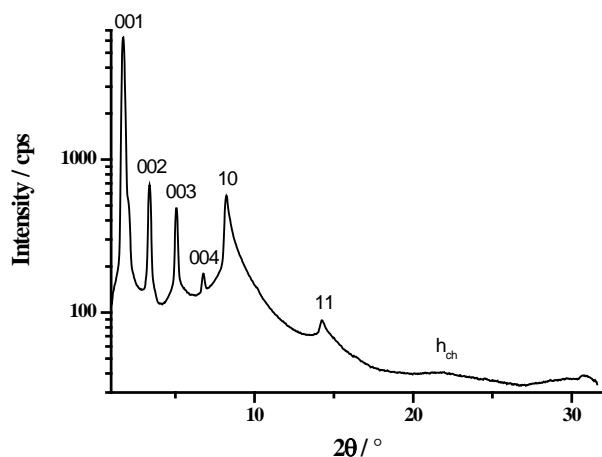


Figure S11. SAXS pattern of **Cplx1** recorded at 140 °C (2<sup>nd</sup> heating curve).

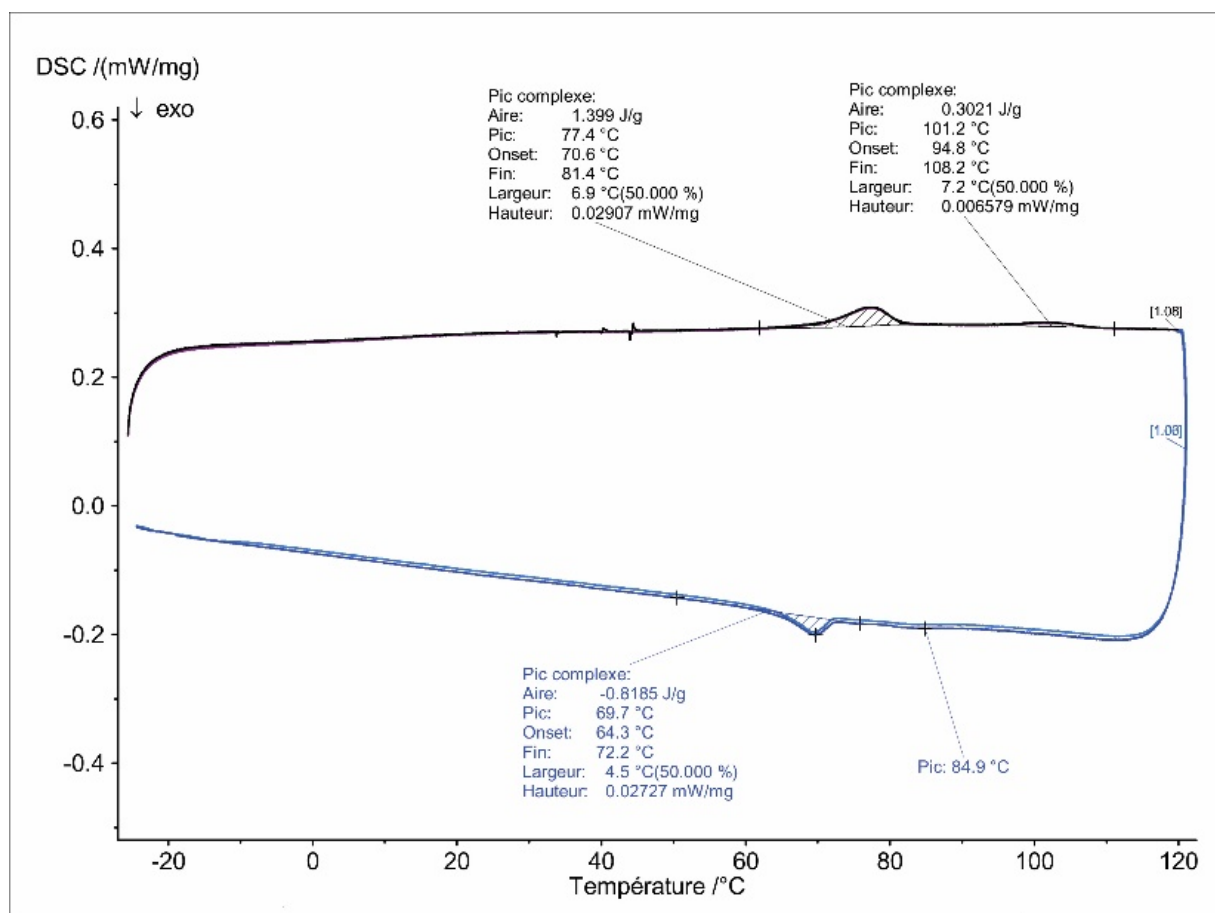
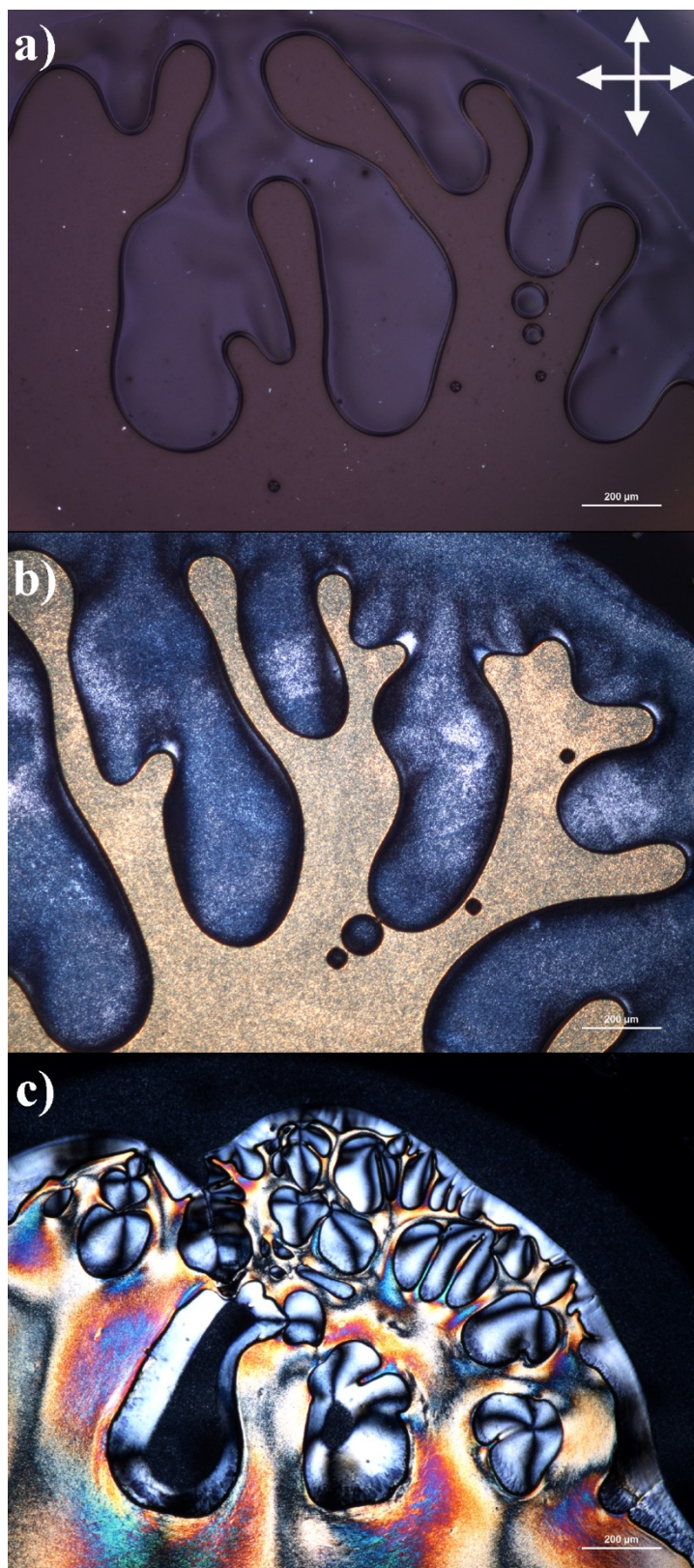
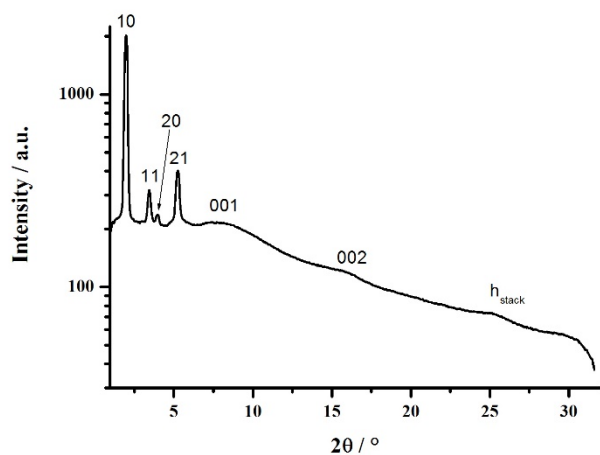


Figure S12. DSC traces of **Cplx2** compound (Top: 2<sup>nd</sup> and 3<sup>rd</sup> heating curves, bottom: 1<sup>st</sup> and 2<sup>nd</sup> cooling curves, scan rate: 10°C/min).



**Figure S13.** Optical photomicrograph of **Cplx2** obtained with a polarizing microscope at: a) 120 °C in the isotropic phase, b) 84 °C upon slow cooling from the isotropic phase and c) 84 °C after gentle pressure on the glass slide (crossed-polarizers symbolized by the white cross in the corner of the picture).



**Figure S14.** SAXS patterns of **Cplx2** recorded at 80 °C.

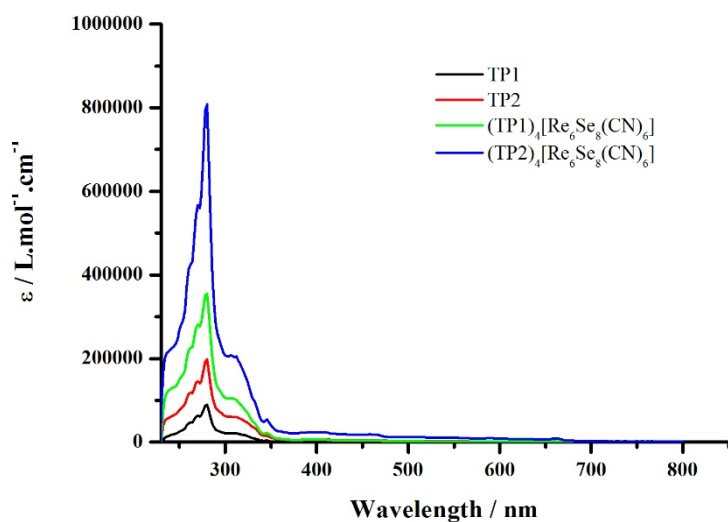


**Figure S15.** Absorption spectra of **TP1Br**, **TP2Br**, **Cplx1** and **Cplx2** in dichloromethane ( $c \sim 10^{-6}$  M)

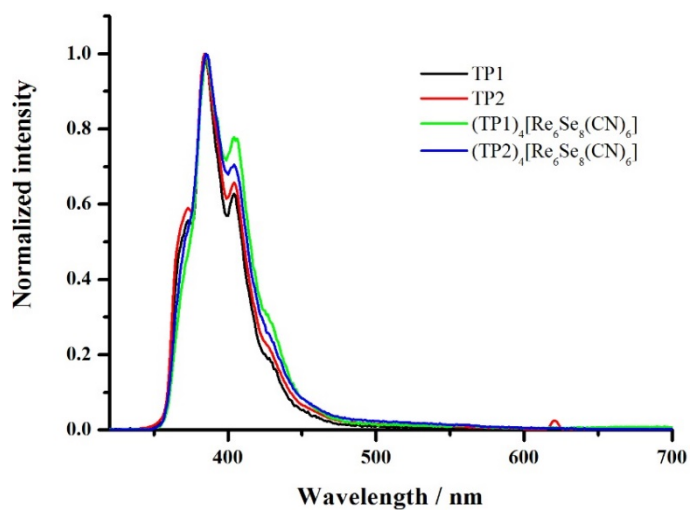


**Figure S16.** Normalized emission spectra in aerated dichloromethane of **TP1Br**, **TP2Br**, **Cplx1** and **Cplx2** upon excitation at 310 nm.

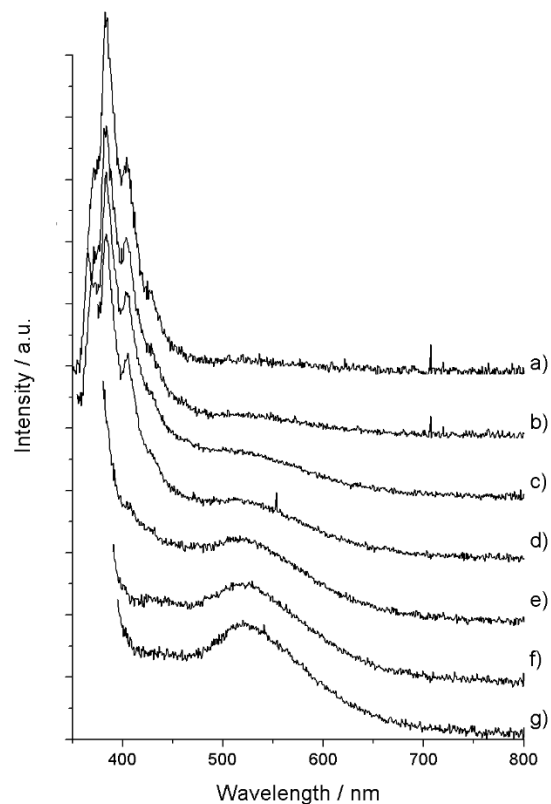


**Figure S17.** Emission spectra in deaerated dichloromethane of **TP1Br**, upon excitation at a) 320 nm, b) 350 nm, c) 360 nm, d) 365 nm, e) 370 nm, f) 375 nm and g) 380 nm.

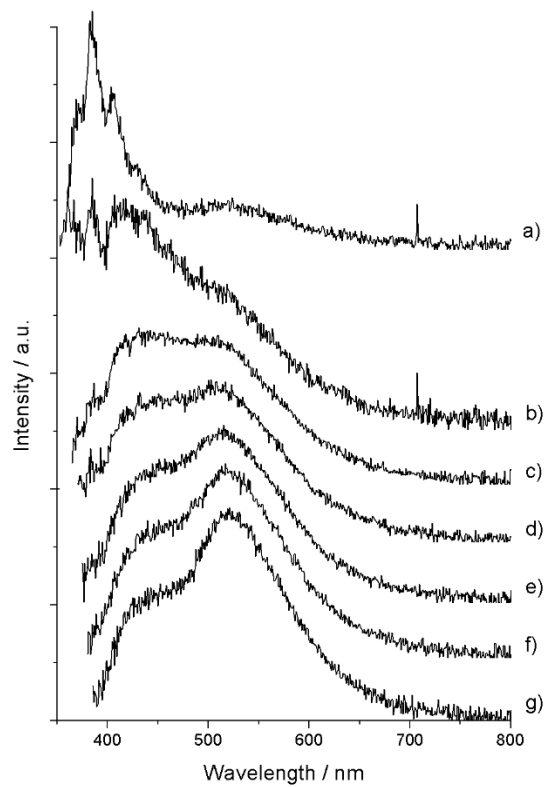


**Figure S18.** Emission spectra in deaerated dichloromethane of **TP2Br**, upon excitation at a) 320 nm, b) 350 nm, c) 360 nm, d) 365 nm, e) 370 nm, f) 375 nm and g) 380 nm.

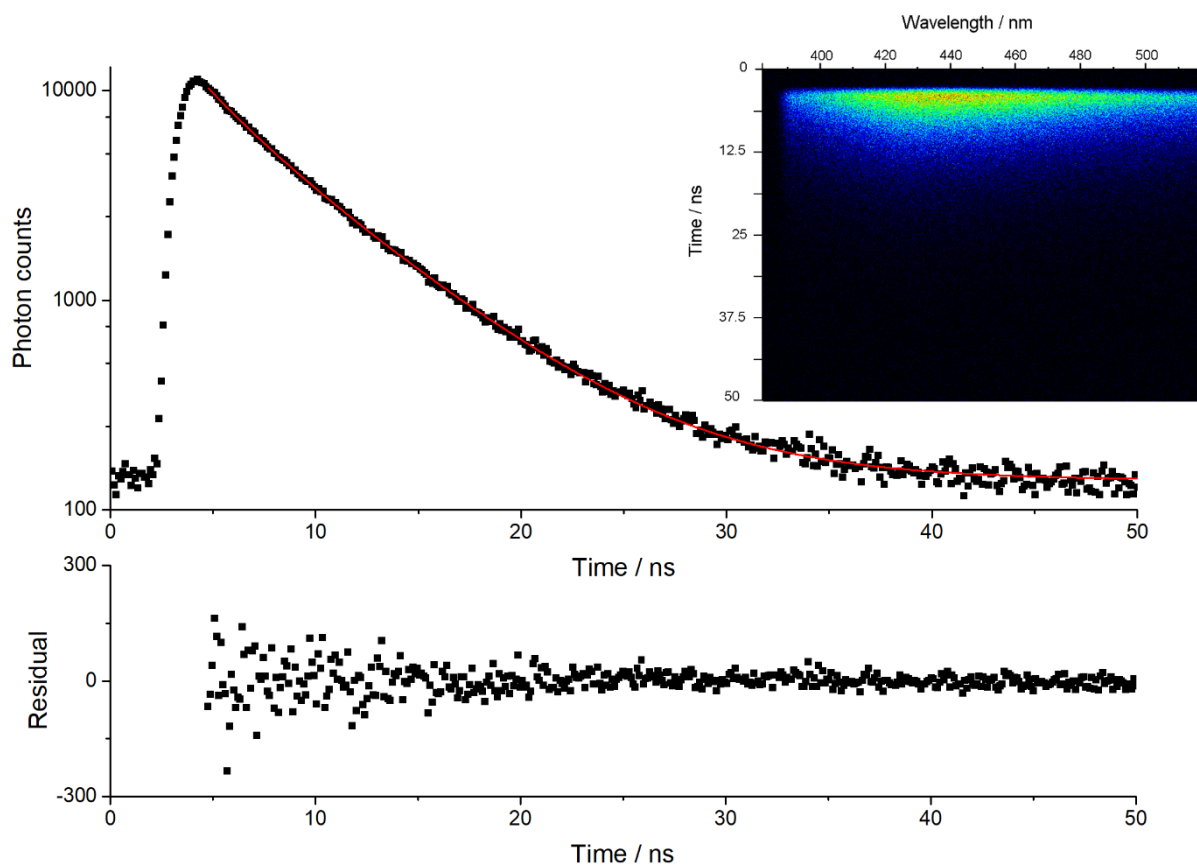


**Figure S19.** Integrated luminescence decay profile of **TP1Br** in dichloromethane; inset: corresponding emission decay map.

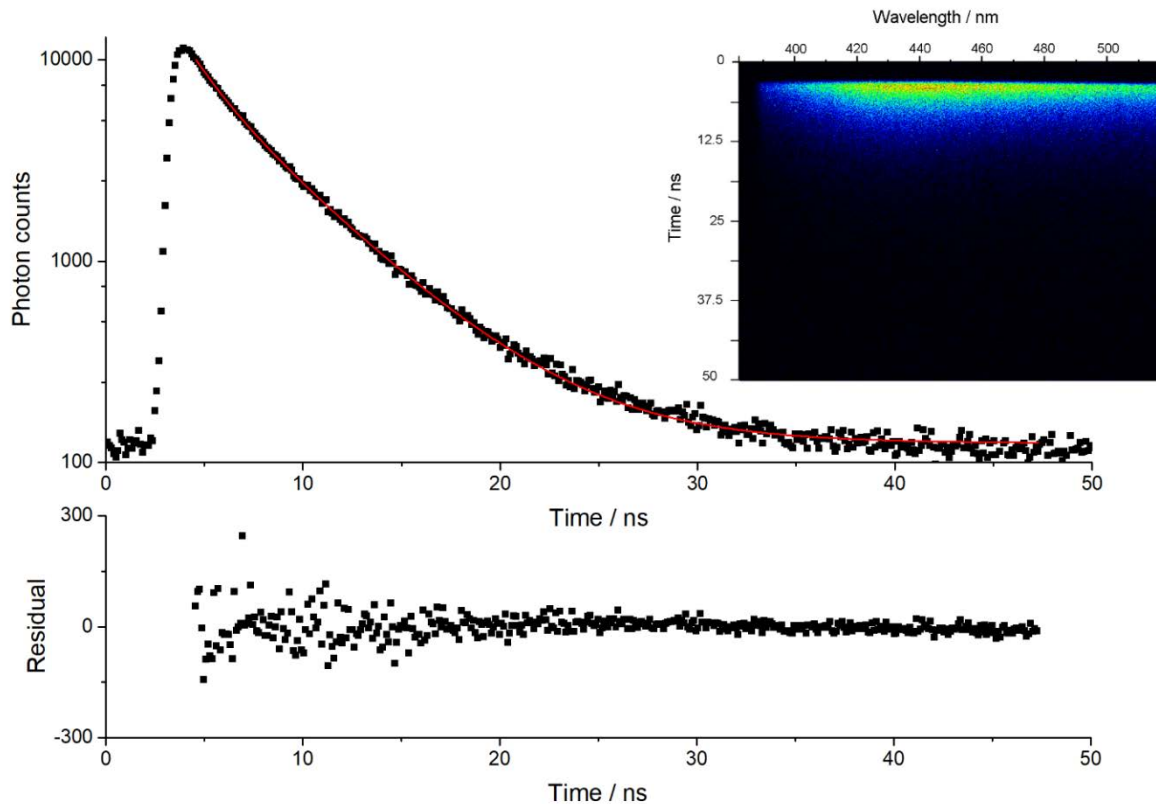


**Figure S20.** Integrated luminescence decay profile of **TP2Br** in dichloromethane; inset: corresponding emission decay map.

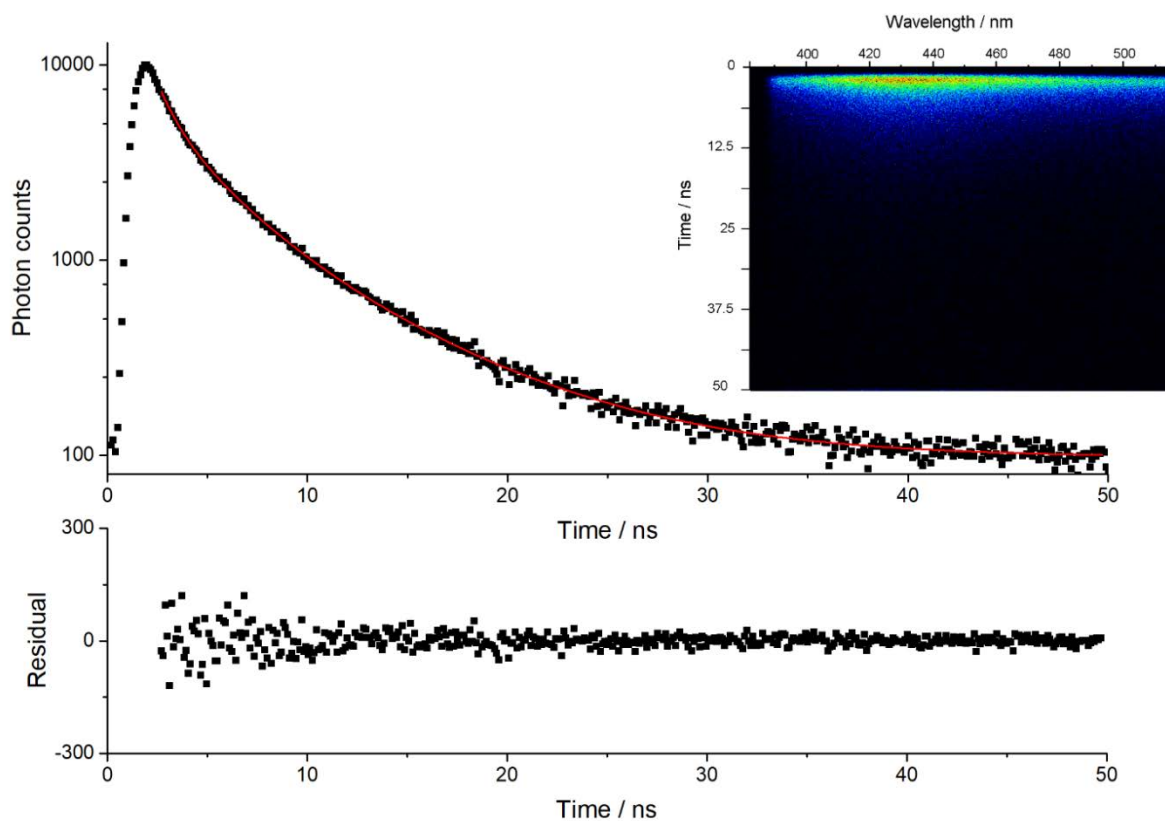


**Figure S21.** Integrated luminescence decay profiles of **Cplx1** in deaerated dichloromethane; inset: corresponding emission decay map between 382 and 518 nm.

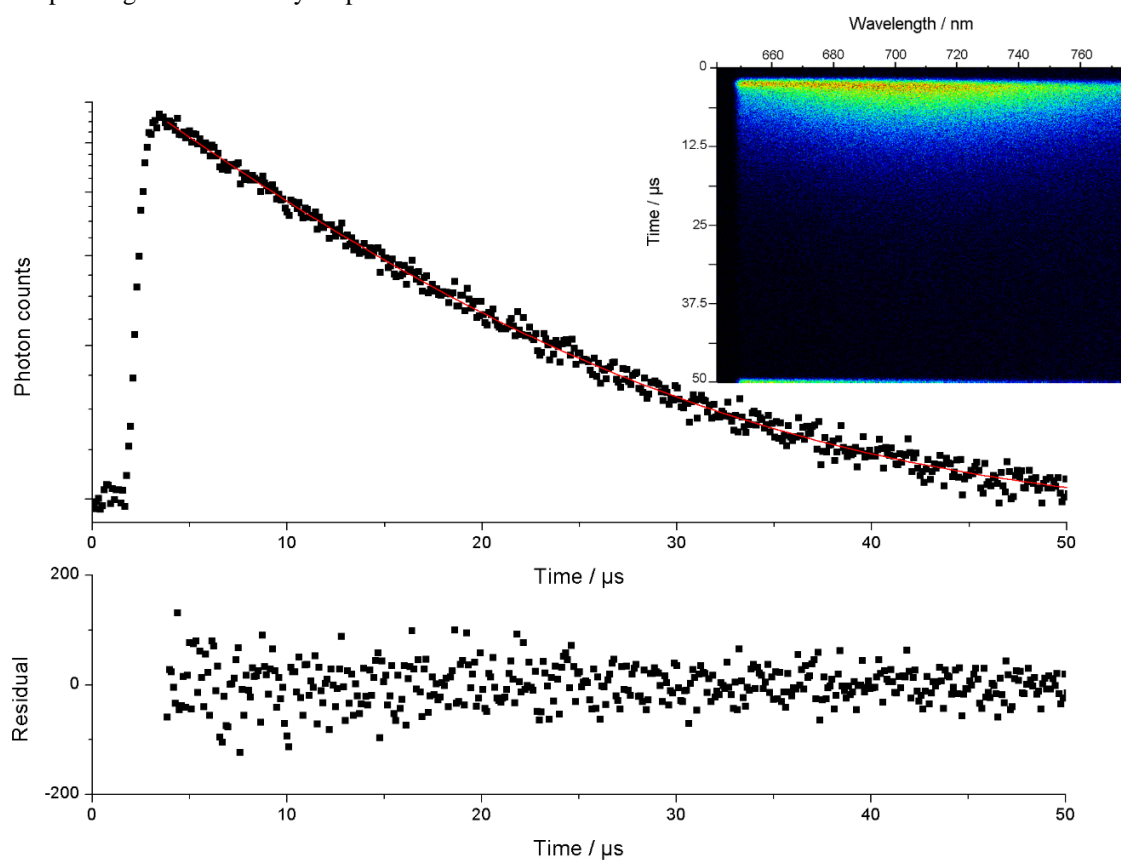


**Figure S22.** Integrated luminescence decay profiles of **Cplx1** in deaerated dichloromethane; inset: corresponding emission decay map between 642 and 778 nm.

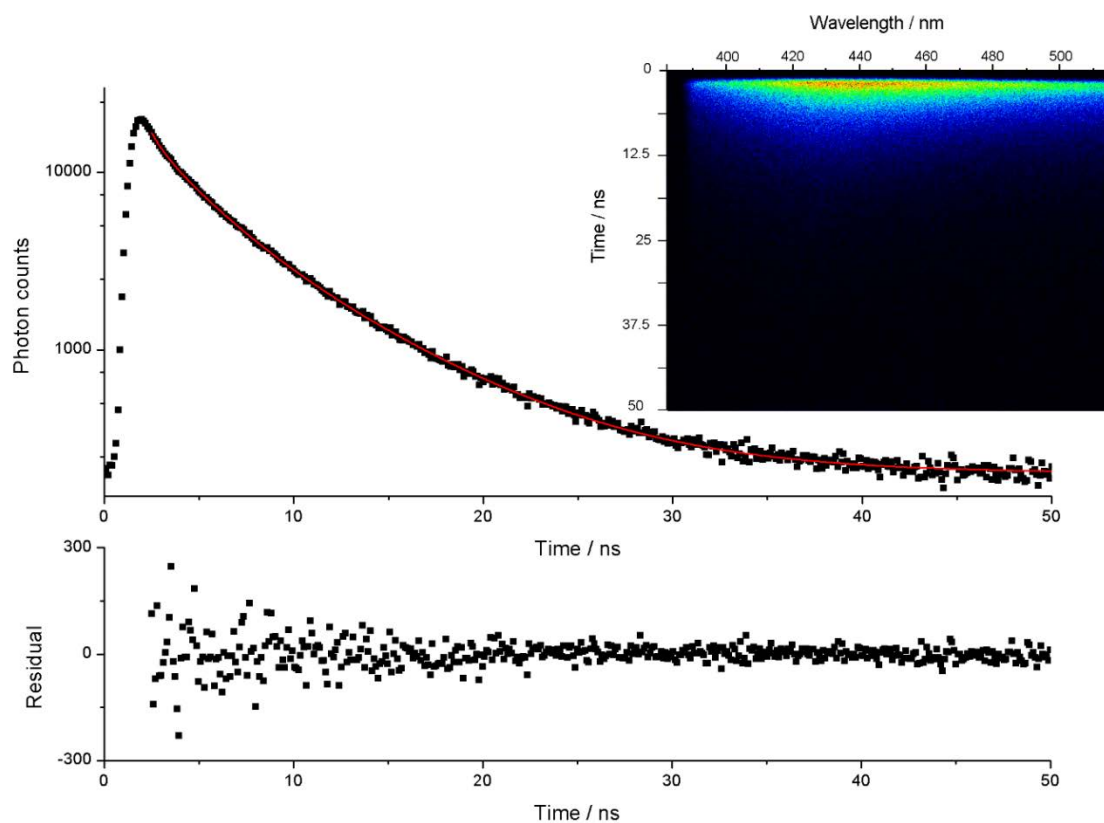


**Figure S23.** Integrated luminescence decay profiles of **Cplx2** in deaerated dichloromethane; inset: corresponding emission decay map between 382 and 518 nm.

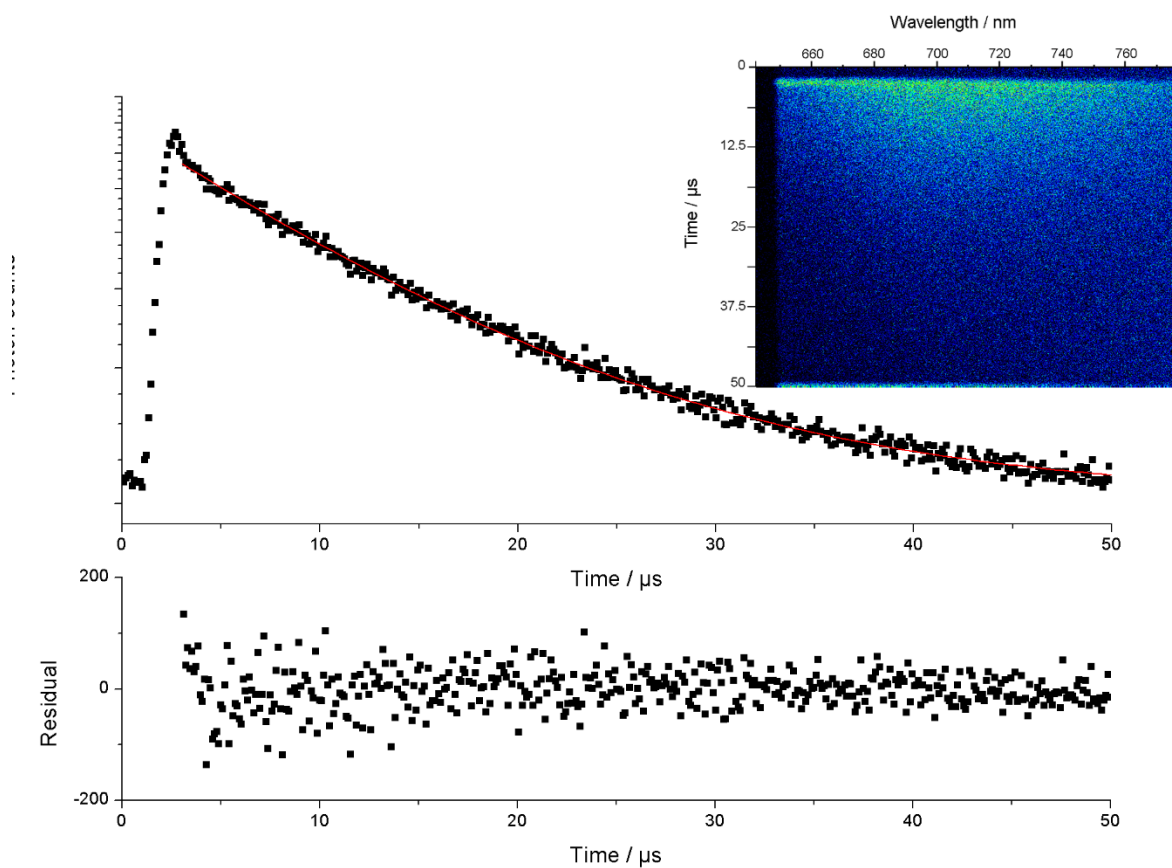


**Figure S24.** Integrated luminescence decay profiles of **Cplx2** in deaerated dichloromethane; inset: corresponding emission decay map between 642 and 778 nm.

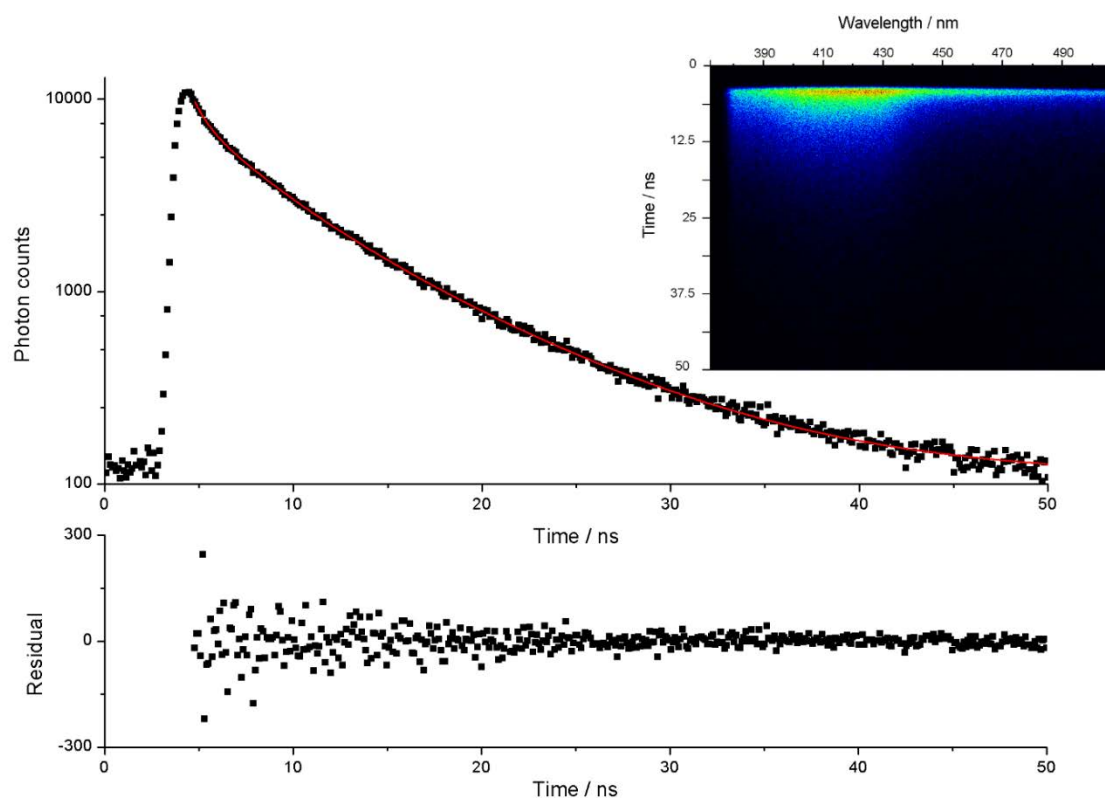


**Figure S25.** Solid state integrated luminescence decay profile of **TP1Br**; inset: corresponding emission decay map.

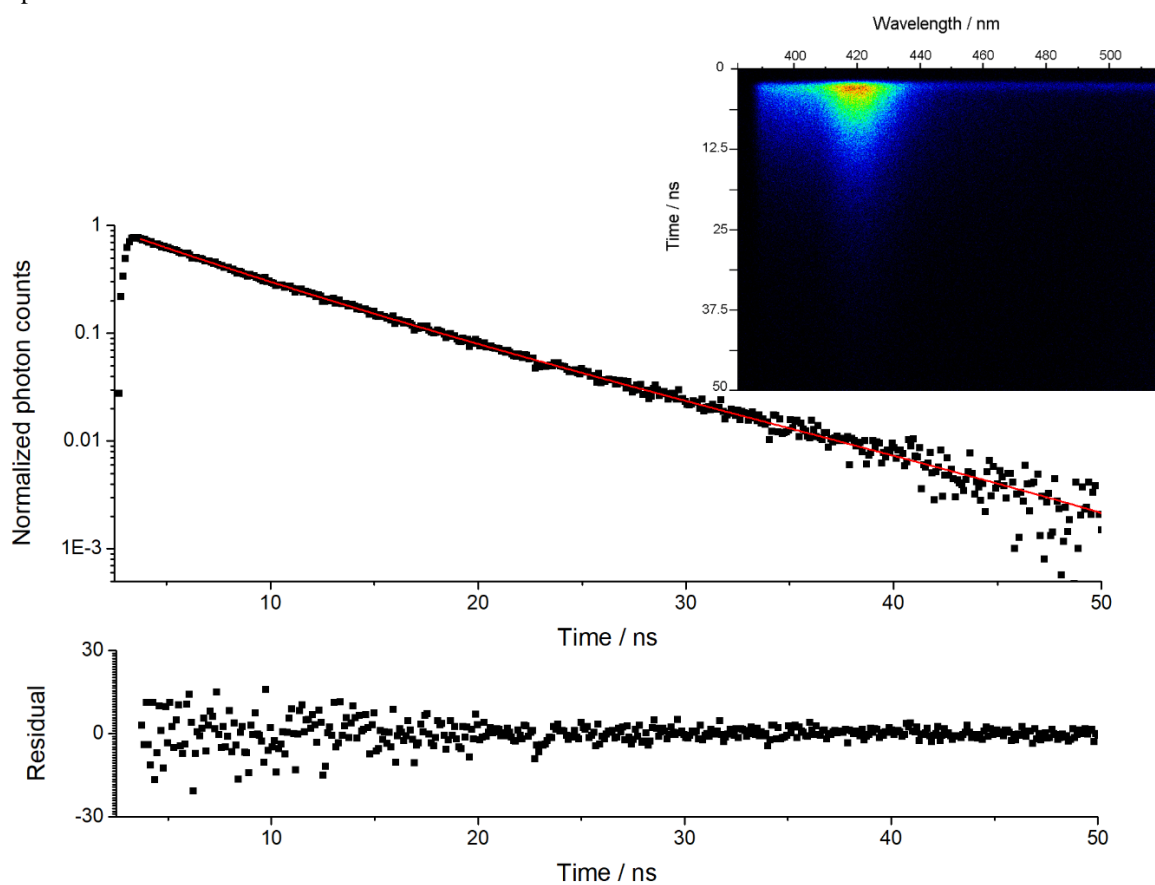


**Figure S26.** Solid state integrated luminescence decay profile of **TP2Br**; inset: corresponding emission decay map.

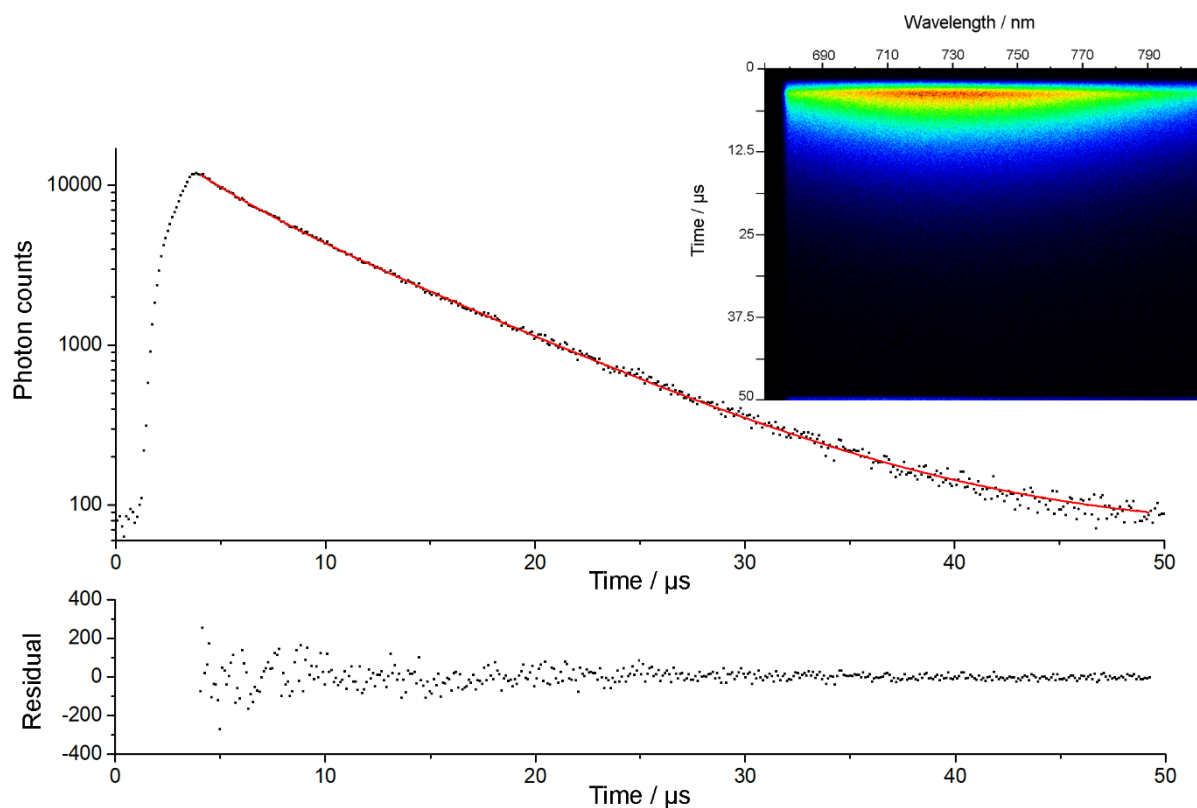


**Figure S27.** Solid state integrated luminescence decay profile of **Cplx1**; inset: corresponding emission decay map.

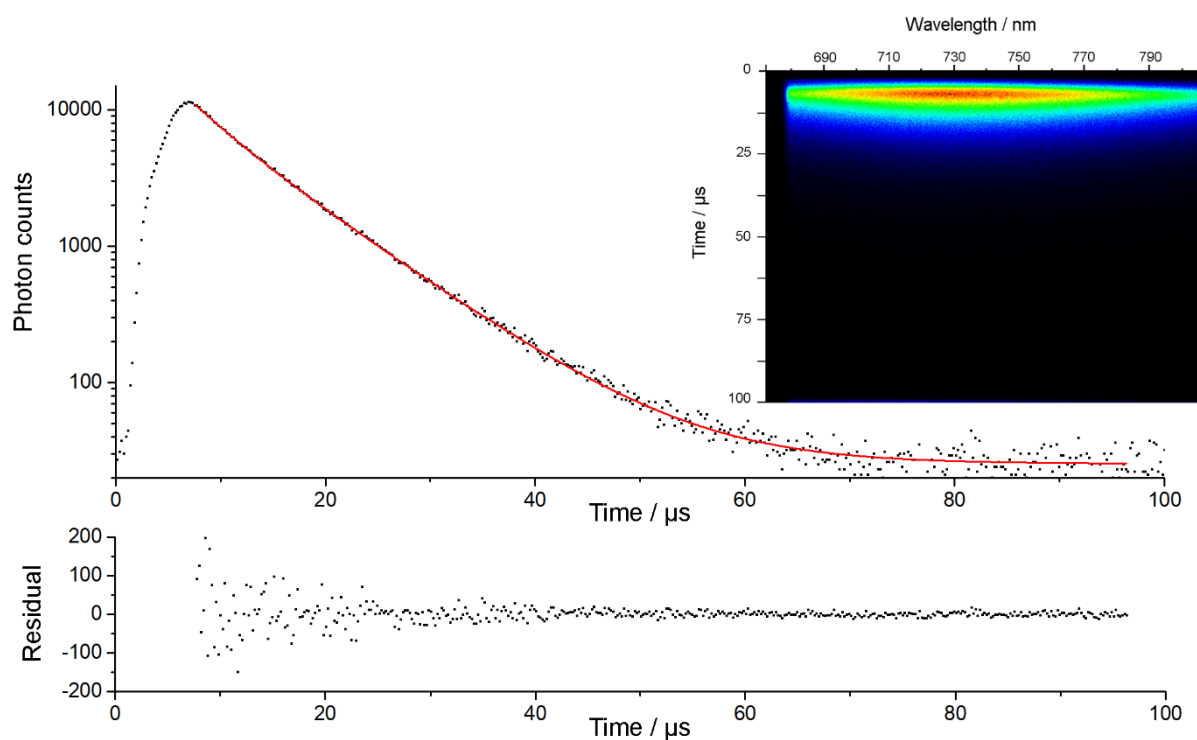


**Figure S28.** Solid state integrated luminescence decay profile of **Cplx2**; inset: corresponding emission decay map.